Ki-67 and CDK1 Control the Dynamic Association of Nuclear Lipids with Mitotic Chromosomes

Hsiao-Tang Hu[1], Ueh-Ting Tim Wang[2,3], Bi-Chang Chen[2], Yi-Ping Hsueh[1]*, Ting-Fang Wang[1]*

[1] Institute of Molecular Biology, Academia Sinica, Taipei, 11529, Taiwan; [2] Research Center for Applied Sciences, Academia Sinica, Taipei 11529, Taiwan; 3 Department of Photonics, National Yang Ming Chiao Tung University, Hsinchu 300093, Taiwan.

* Corresponding to Dr. Ting-Fang Wang, email: tfwang@gate.sinica.edu.tw and Dr. Yi-Ping Hsueh, Email: yph@gate.sinica.edu.tw, Institute of Molecular Biology, Academia Sinica, 128, Sec 2, Academia Rd, Taipei, 11529, Taiwan, ROC.

Keywords: Biotin-DHPE, Cell cycle, Cell cycle-dependent kinase 1, Expansion microscopy, Ki-67, Nuclear lipid, Perichromosomal layer, Phosphatidylserine, TT-ExM.

Abstract

Nuclear lipids play roles in regulatory processes such as signaling, transcriptional regulation, and DNA repair. In this report, we demonstrate that nuclear lipids may contribute to Ki-67-regulated chromosome integrity during mitosis. In COS-7 cells, nuclear lipids are enriched at the perichromosomal layer and excluded from intrachromosomal regions during early mitosis, but are then detected in intrachromosomal regions during late mitosis, as revealed by TT-ExM, an improved expansion microscopy technique that enables high-sensitivity, super-resolution imaging of proteins, lipids, and nuclear DNA. The nuclear non-histone protein Ki-67 acts as a surfactant to form a repulsive molecular brush around fully condensed sister chromatids in early mitosis, preventing the diffusion or penetration of nuclear lipids into intrachromosomal regions. Ki-67 is phosphorylated during mitosis by cyclin-dependent kinase 1 (CDK1), the best-known master regulator of the cell cycle. Both Ki-67 knockdown and reduced Ki-67 phosphorylation by CDK1 inhibitors allow nuclear lipids to penetrate chromosomal regions. Thus, both Ki-67 protein level and phosphorylation status during mitosis appear to influence the perichromosomal distribution of nuclear lipids. Ki-67 knockdown and CDK1 inhibition also lead to uneven chromosome disjunction between daughter cells, highlighting the critical role of this regulatory mechanism in ensuring accurate chromosome segregation. Given that Ki-67 has been proposed to promote chromosome individualization during open mitosis in vertebrates, our results reveal that nuclear lipid enrichment at the perichromosomal layer enhances Ki-67's ability to form a protective chromosomal envelope, which is critical for correct chromosome segregation and maintenance of genome integrity during mitosis.

Introduction

Lipids are key biomolecules that form the structures of biomembranes and serve as signaling molecules to regulate cellular responses. In the nucleus, neutral and polar lipids are found in the nuclear envelope (NE), nucleolus, and nuclear matrix (Ledeen and Wu, 2008, Garcia-Gil and Albi, 2017, Moriel-Carretero, 2021). These lipids can be synthesized *de novo* in the inner nuclear membrane and nuclear matrix or generated at the endoplasmic reticulum connected to the NE and transported into the nucleus (Payrastre et al., 1992, Vann et al., 1997, Romanauska and Köhler, 2018, Fujimoto, 2022). Some nuclear lipids form droplets that serve as nucleolar scaffolding structures, splicing speckles, and DNA repair foci (Osborne et al., 2001, Mortier et al., 2005, Wang et al., 2017). In addition to serving as structural components, nuclear lipids also participate in a variety of biological functions, including in transcriptional regulation (Zou et al., 2011, Yildirim et al., 2013, McDonnell et al., 2016), signaling (Wang et al., 2017, Zhang et al., 2007, Yildirim et al., 2013), the DNA damage response (Wang et al., 2017, Zhang et al., 2007), and protein storage (Cermelli et al., 2006, Kumanski et al., 2021). Therefore, nuclear lipids have multiple activities.

Ki-67, a giant nuclear non-histone protein comprising 3256 amino acids, is a well-known marker of cell proliferation (Andrés-Sánchez et al., 2022). The subnuclear distribution of Ki-67 changes significantly during the cell cycle (Sun and Kaufman, 2018). Ki-67 is concentrated in the nucleolus and in some punctate structures during interphase, but it relocates to transparent gel-like structures surrounding condensed chromosomes (termed the perichromosomal layer or chromosomal periphery) during mitosis (Kill, 1996, Booth and Earnshaw, 2017, Sun and Kaufman, 2018, Gautier et al., 1992). Based on analyses of Ki-67, the perichromosomal layer is thought to isolate (or individualize) sister chromatid pairs from other pairs and to promote efficient

interactions with the mitotic spindle during mitosis (Cuylen et al., 2016). Ki-67 also excludes the cytoplasm from condensed chromosomes during mitosis (Cuylen-Haering et al., 2020).

The perichromosomal layer mostly originates from the nucleolus (Booth and Earnshaw, 2017, Ma et al., 2007). When a cell enters mitosis, the nucleolus dissipates and its components relocate to cover the surface of mitotic chromosomes (Booth and Earnshaw, 2017, Ma et al., 2007). In addition to Ki-67, other nucleolar components, including nucleolin and ribosomal RNA, are present in the perichromosomal layer (Hsu et al., 1965, Moyne and Garrido, 1976, Ma et al., 2022). These proteins and RNA molecules form a liquid-like coat on mitotic chromosomes and regulate chromosome behavior during mitosis (Hernandez-Armendariz et al., 2024). Although the nucleolus also contains lipids (Wang et al., 2017, Guillen-Chable et al., 2021, Morovicz et al., 2022), it is currently unclear if nucleolar lipids also relocate to the perichromosomal layer and functionally contribute to this interesting biological process. Thus, whether nuclear lipids are present or even enriched at the perichromosomal layer remains elusive.

Expansion microscopy (ExM) is a super-resolution imaging technology that physically expands biological samples by a factor of four or greater, thereby improving the spatial resolution of optical microscopy (Chen et al., 2015, Wassie et al., 2019, Wang et al., 2023, Hu et al., 2023). The biological sample is first embedded in a hydrogel and then physically crosslinked within it before undergoing protease digestion. The biological sample then expands isotropically with the hydrogel when placed in water (Chen et al., 2015, Wassie et al., 2019). Since its original description, many variations of the ExM protocol have been developed to achieve a resolution comparable to those of electron microscopy, including iterative expansion microscopy (iExM) (Chang et al., 2017), pan-ExM (M'Saad and Bewersdorf, 2020), and iterative ultrastructure

83 expansion microscopy (iU-ExM) (Louvel et al., 2023). However, concerns have arisen regarding
84 the use of these iterative methods to visualize membranes or lipid-containing subcellular structures
85 due to their use of strong lytic and denaturing reagents such as sodium dodecyl sulfate (SDS)
86 and/or sodium hydroxide (NaOH) (Chang et al., 2017, M'Saad and Bewersdorf, 2020, Louvel et
87 al., 2023).

88 To visualize both proteins and lipids of cultured mammalian cells at a super-resolution
89 scale, we established a modified protocol called TT-ExM that involves application of trypsin and
90 tyramide signal amplification (TSA) technologies. We have demonstrated previously that
91 trypsinization retains convincing fluorescent signals in ExM (Hu et al., 2023, Wang et al., 2023).
92 A combination of a biotin-conjugated lipid, i.e., biotin-DHPE (N-(Biotinoyl)-1,2-dihexadecanoyl-
93 sn-glycero-3-phosphoethanolamine), and TSA technology clearly labeled the membranes and
94 lipid-containing structures of cells, including mitochondria, the nuclear envelope (NE),
95 endoplasmic reticulum, Golgi apparatus, lipid-containing vesicles in the cytoplasm, and lipid-
96 containing foci in the nucleolus (Wang et al., 2023). Notably, we have shown that our system
97 reveals the localization of intranuclear lipid components at the perichromosomal layer of mitotic
98 chromosomes (Wang et al., 2023). Accordingly, we speculate that nuclear lipids are involved in
99 forming the perichromosomal layer. In this report, we deploy TT-ExM to illustrate the
100 ultrastructural organization of the perichromosomal layer by revealing the distributions of lipids
101 and Ki-67 during the cell cycle. Our results indicate that Ki-67 regulates the distribution of nuclear
102 lipids at the perichromosomal layer and intrachromosomal region in a cell cycle-dependent manner.
103 Ki-67 knockdown or reducing Ki-67 phosphorylation by means of a CDK1 inhibitor disrupts the
104 distribution of nuclear lipids at the perichromosomal layer. During mitosis, ki-67 and nuclear lipids
105 may act in concert to segregate or individualize the various sister chromatid pairs.

106

107 ## Results

108 **Application of TT-ExM to observe lipid-containing structures and chromosomes**

109 We used Biotin-DHPE and tyramide-Alexa fluor-555 in TT-ExM to label and visualize nuclear
110 lipids in COS-7 cells (Wang et al., 2023). After crosslinking to a hydrogel and trypsinization, the
111 sample swells upon immersion in water. PicoGreen, an ultrasensitive green-fluorescent nucleic
112 acid dye for double-stranded DNA, was used to outline nuclear chromosomal DNA. As previously
113 described (Wang et al., 2023), after 4-fold expansion, both cytoplasmic components and nuclear
114 structures of COS-7 cells expanded isotropically, regardless of their cell cycle stages (**Figure 1A**
115 post-expansion). Lipid-containing structures in the cytoplasm, nuclei (e.g., NEs), and nucleoli
116 were clearly labeled by biotin-DHPE (**Figure 1A**), confirming the feasibility of deploying biotin-
117 DHPE in TT-ExM to reveal cellular lipid structures. Notably, biotin-DHPE signals were present
118 in the peripheral regions of mitotic chromosomes (**Figure 1A**, middle magnified inset), suggesting
119 the presence of lipids in the perichromosomal layer. All images above were viewed using a Zeiss
120 LSM700 confocal laser scanning microscope.

121 To further confirm the lipid signals labeled by DHPE-biotin, we applied organic solvents
122 to extract lipids from paraformaldehyde-fixed cells. After paraformaldehyde fixation and before
123 adding DHPE-biotin, we extracted the lipids by adding methanol or acetone according to
124 methodologies described previously (DiDonato and Brasaemle, 2003, Vore et al., 1974). We found
125 that either the methanol or acetone treatment reduced DHPE-biotin signals by more than 70%
126 when compared to paraformaldehyde fixation alone (**Figure 1B, 1C** upper). In addition to DHPE-
127 biotin staining, DNA counterstaining with 4',6-diamidino-2-phenylindole (DAPI) and
128 immunofluorescence staining using anti-Ki-67 antibody were also conducted to validate the

129 specific effect of methanol or acetone treatment on lipid extraction (**Figure 1B, 1C**). DAPI is a
130 blue fluorescent DNA stain for which fluorescence is enhanced ~20-fold upon binding to AT-
131 enriched regions of double-stranded DNA. Ki-67 signals represent nuclear proteins surrounding
132 mitotic chromosomes during cell division. We found that the DHPE-biotin signals were generally
133 reduced in all subcellular regions following the methanol or acetone treatment (**Figure 1B, 1C**).
134 However, the same treatments did not affect chromosomal DNA or nuclear Ki-67 protein (**Figure**
135 **1B, 1C**), supporting the specific effect of methanol and acetone in removing lipids. These results
136 confirm that DHPE-biotin indeed specifically labels lipids in cells.

137 Next, we applied a Zeiss LSM980 confocal laser scanning microscope with an AiryScan 2
138 area detector to acquire super-resolution images of COS-7 cells stained with DAPI. To quantify
139 the fluorescence signals, we drew a perpendicular line across the chromosome periphery of sister
140 chromatid pairs that had fully condensed during mitosis and performed a line scan analysis of
141 DAPI signals along that line (**Figure 2A**). The expansion index of TT-ExM was determined by
142 comparing the average diameter of fully condensed sister chromatid pairs (**Figure 2B**). Our results
143 show that the average diameters before and after expansion were 1.4 μm and 4.9 μm, respectively,
144 representing an expansion index of 3.5 (**Figure 2C**). Since the LSM980 microscope with AiryScan
145 2 has a resolution of approximately 90-120 nm, we estimate that the resolution of our TT-ExM
146 protocol is 25-34 nm after 3.5-fold expansion (Hu et al., 2023). Under the same conditions,
147 counterstaining with PicoGreen revealed the highly condensed chromosome axis in the middle of
148 each sister chromatid (indicated by white arrows in **Figure 2D,** right panel). Notably, the surfaces
149 of most, if not all, individual chromatids during mitosis did not appear smooth, suggesting that
150 fully folded chromosomal loops could be observed under our super-resolution conditions
151 (indicated by white asterisks in **Figure 2D**, right panel). These results indicate that TT-ExM is

suitable for isotropic expansion of biological macromolecules (e.g., mitotic chromosomes), allowing us to accurately observe the ultrastructures of organelles and subcellular components under an optical microscope.

Dynamic distribution of nuclear lipids during mitosis

We further investigated the distribution of lipid components at the perichromosomal layers. In addition to biotin-DHPE, we dual-stained the cells with an anti-Ki-67 antibody (**Figure 3**) and an anti-phosphatidylserine (PS) antibody (**Figure 4**). Ki-67 is a critical component in forming and organizing the perichromosomal layers (Cuylen et al., 2016, Cuylen-Haering et al., 2020, Ma et al., 2022). It also controls chromosome individualization and genome stability during mitosis (Takagi et al., 2014, Takagi et al., 2018, Garwain et al., 2021, Stamatiou et al., 2024). PS is an anionic glycerophospholipid. Immunofluorescence signals of anti-PS antibodies specifically localize in epichromatin throughout the cell cycle and are associated with nucleosome core histones (Prudovsky et al., 2012). In fixed and permeabilized cells, epichromatin can be identified by partial co-immunolocalization of Ki-67 with staining signals of particular anti-nucleosome or anti-PS antibodies (Gould et al., 2017).

We observed that the immunofluorescence signals of biotin-DHPE indeed overlapped with those of Ki-67 at the perichromosomal layers during prometaphase and metaphase (**Figure 3A**). As mitosis progressed into anaphase and telophase, we detected enhanced biotin-DHPE immunofluorescence signals in the chromosomal interior regions. These results indicate that DHPE-labeled nuclear components (e.g., nuclear lipids) had migrated from the perichromosomal layers toward chromosomal cores as mitosis progressed (**Figure 3A**).

174 To quantify the movement of the biotin-DHPE signals toward the chromosomal interior,
175 we performed line scanning as described in Figure 2 to determine the ratio between the lowest
176 biotin-DHPE signal within chromosomes and the biotin-DHPE signal at chromosome edges, i.e.,
177 the inner/edge ratio of DHPE signal (**Figure 3B**). Our results show that this ratio is less than 0.4
178 during prometaphase and metaphase, but increases to ~0.5 and ~0.6 for anaphase and telophase,
179 respectively (**Figure 3C**). By quantifying average global Ki-67 immunofluorescence signals in
180 mitotic cells, we also detected that intracellular Ki-67 levels decline as mitosis progresses from
181 prometaphase to telophase (**Figure 3D**). Given that we uncovered a significant negative correlation
182 between intracellular Ki-67 protein levels and the inner/edge ratio of DHPE signals (**Figure 3E**),
183 we speculate that Ki-67 may prevent DHPE-labeled nuclear components (e.g., nuclear lipids) from
184 moving into chromosomal interiors during prometaphase and metaphase, thereby promoting
185 chromosome individualization.
186
187 **Perichromosomal lipid composition and layer organization**
188 Consistent with the previous study (Prudovsky et al., 2012), we also found that PS
189 immunoreactivity specifically localized in epichromatin after specimen expansion (**Figure 4A**,
190 upper). Z-projection images revealed that PS signal specifically occurred on the surface of the
191 mitotic chromosome cluster during prometaphase (**Figure 4A**, lower). This pattern differs from
192 that of biotin-DHPE signals, which surrounded the mitotic chromosomes (**Figure 4A and 4B**).
193 However, biotin-DHPE signals overlapped with the PS signals within the epichromatin region
194 (**Figure 4B**). Our line scan analysis indicated that the peak of PS signals was closer to the edge of
195 mitotic chromosomes compared to the peak of biotin-DHPE signals (**Figure 4C**). Taken together,

196 these results indicate that, in addition to PS, other lipid components are also enriched around
197 chromosomes.

198 We also analyzed the relative positions of the signal peaks for Ki-67 and biotin-DHPE.
199 Similar to our comparison of PS and biotin-DHPE, we found that the peak of Ki-67 signals was
200 closer to the edge of mitotic chromosomes compared to the peak of biotin-DHPE signals (**Figure**
201 **4D, 4E**). Thus, the DHPE-labeled lipid layer appears to be located outside of the Ki-67 layer of
202 the perichromosomal zone. This scenario is consistent with our hypothesis that Ki-67 may prevent
203 inward movement of lipid components into the interior of mitotic chromosomes.

204

205 **Ki-67 knockdown causes chromosome aggregation, slows cell cycle progression, and alters**
206 **the pattern of the microtubule array**

207 To further confirm the role of Ki-67 in controlling lipid distribution across chromosomes and the
208 perichromosomal layer, we studied the effect of Ki-67 knockdown in COS-7 cells. To establish
209 and characterize Ki-67 knockdown, we designed a plasmid expressing an artificial miRNA, Ki67-
210 miR, to downregulate endogenous Ki-67 in COS-7 cells. Immunostaining and immunoblotting
211 revealed that Ki67-miR significantly reduced Ki-67 protein levels in COS-7 cells relative to the
212 control construct Ctrl-miR (**Figure 5A-5C**). Consistent with previous studies (Cuylen et al., 2016,
213 Cuylen-Haering et al., 2020), Ki-67 knockdown prompted mitotic chromosome collapse and
214 aggregation (**Figure 5A**, as revealed by DAPI counterstaining). Quantification analysis revealed
215 that the area occupied by chromosomes was diminished in Ki-67 knockdown cells compared to
216 cells expressing Ctrl-miR (**Figure 5D**). These results demonstrate that we had successfully
217 knocked down Ki-67 and impaired the spatial arrangement of mitotic chromosomes in COS-7
218 cells.

219 Ki-67 knockdown also delayed the progress of mitosis. First, we applied nocodazole to
220 arrest control or Ki-67 knockdown COS-7 cells at prometaphase (**Figure 5E**, left panel). After
221 washing away nocodazole and allowing the cells to recover for 15, 30, or 60 minutes, we then
222 counted the numbers of COS-7 cells at different stages of mitosis (i.e., prometaphase, metaphase,
223 anaphase, and telophase). Within 15 minutes of washing away nocodazole, more than 30% of the
224 control cells progessed from prometaphase into metaphase. By comparison, only 10% of the Ki-
225 67 knockdown cells entered metaphase under the same treatment (**Figure 5E**). Furthermore, less
226 than 10% of Ctrl-miR- and Ki67-miR-expressing cells remained in prometaphase 60 minutes after
227 nocodazole had been washed away, with ~40% of the Ctrl-miR-expressing cells entering telophase.
228 In contrast, only 20% of Ki67-miR-expressing cells progressed to telophase. We detected a slight
229 increase in the percentages of Ki-67 knockdown cells in metaphase and anaphase (**Figure 5E**,
230 right). Therefore, Ki-67 knockdown delays mitotic progression.

231 In addition to chromosomes, we also monitored microtubule patterns in cells expressing
232 Ki67-miR. Since microtubule patterns change during the different stages of mitosis, we focused
233 on the microtubule array in early prometaphase for our comparison (**Figure 6**). At this stage of
234 mitosis, microtubules form a star-like pattern in the center of the chromosome cluster. We observed
235 microtubule filaments extending from the center to the periphery of the chromosome cluster in
236 control COS-7 cells (**Figure 6A**, upper). However, mitotic chromosomes collapsed in Ki67-miR-
237 expressing cells, so although microtubules still formed a star-like pattern in the center of the
238 chromosome cluster of those cells, the star-like pattern was smaller and more irregular than for
239 control counterparts (**Figure 6A**, lower). To quantify the differences, we performed Sholl analysis
240 (Sholl, 1953) to analyze the complexity of microtubules in early prometaphase of control and Ki-
241 67 knockdown cells (**Figure 6B**). Our Sholl analysis revealed that the number of intersections was

242 greatly reduced in Ki-67 knockdown cells (**Figure 6C**), i.e., less than 50% of that enumerated for
243 control cells (**Figure 6D**). We further counted all microtubule filament tips to represent the total
244 number of microtubule filaments in each array, which revealed ~50% fewer microtubule tips in
245 Ki-67 knockdown cells compared to control cells (**Figure 6E**). Thus, Ki-67 knockdown induces
246 microtubule array abnormalities during mitosis.

247 Consequently, Ki-67 is critical for chromosome elongation and individualization during
248 mitosis, both of which are required for microtubule attachment to chromosomes to enable mitotic
249 progression.

250

251 **Ki-67 knockdown promotes lipid invasion into condensed chromosomes**

252 Lastly, we applied our Ki-67 knockdown system to investigate if Ki-67 is involved in the inward
253 movement of lipids into the chromosome interior during mitosis. Since we detected biotin-DHPE
254 signals as being lowest within condensed chromosomes during prometaphase compared to other
255 mitotic stages (**Figure 3**), we solely analyzed the effects of Ki-67 knockdown during
256 prometaphase. Given that our miR expression construct coexpresses green fluorescent protein
257 (GFP), we used GFP signal to identify transfected cells in culture (**Figure 7A**). Next, we performed
258 line scans to determine biotin-DHPE signals across chromosomes and the perichromosomal layer.
259 GFP signal was included as a control (**Figure 7B, 7C**). We found that the GFP inner/edge ratio
260 was identical (~0.2) for cells expressing either Ctrl-miR or Ki67-miR (**Figure 7D**), indicating that
261 GFP distribution is insensitive to Ki-67 knockdown. In terms of biotin-DHPE signals, the ratio for
262 control cells was ~0.28, whereas this ratio increased to 0.34 for Ki-67 knockdown cells (**Figure**
263 **7D**), indicating that Ki-67 regulates lipid invasion into condensed chromosomes during mitosis.

264

265 **Blockade of CDK1 activity influences Ki-67 phosphorylation, nuclear lipid distribution and**
266 **chromosome segregation**

267 To further investigate the relationship among the cell cycle, Ki-67 and nuclear lipid distribution,
268 we applied RO-3306, a specific inhibitor of cyclin-dependent kinase 1 (CDK1), to our culture
269 (**Figure 8A**). CDK1 is an essential protein kinase for cell division (Diril et al., 2012, Massacci et
270 al., 2023). It heavily phosphorylates Ki-67 during mitotic entry (Saiwaki et al., 2005, Takagi et al.,
271 2014, Stamatiou and Vagnarelli, 2021), and regulates Ki-67 localization, especially at the
272 perichromosomal layer, during mitosis (Booth et al., 2014, Booth and Earnshaw, 2017, Remnant
273 et al., 2021, Yamazaki et al., 2022). Our RO-3306 treatment efficiently reduced Ki-67
274 phosphorylation levels during mitosis (**Figure 8B**). Next, we added RO-3306 into COS-7 cell
275 culture that had been arrested at prometaphase by means of nocodazole (**Figure 8A**). Compared
276 with vehicle control, the RO-3306 treatment altered mitotic progression after nocodazole washout,
277 with the percentages of cells that stayed at prometaphase or anaphase increasing after RO-3306
278 treatment for 30 min (**Figure 8C**). In contrast, fewer cells were at metaphase upon RO-3306
279 treatment (**Figure 8C**). These results confirm the effect of CDK1 on Ki-67 phosphorylation and
280 mitotic progression.

281 Similar to Ki-67 knockdown, we found that chromosomes were collapsed and aggregated
282 after RO-3306 treatment (**Figure 8D**, inset). RO-3306 not only resulted in a reduction in total
283 chromosome area (**Figure 8E**, left), but also altered microtubule organization. In contrast to Ki-
284 67 knockdown that reduced the number and size of microtubule arrays at prometaphase (**Figure**
285 **6**), RO-3306 treatment dramatically reduced the number of cells displaying the typical organized
286 star-shaped microtubule arrays, with many of the remaining cells instead displaying extended, two-
287 star, or disorganized microtubule arrays (**Figure 8D, 8E**).

288 Consistent with our observations of microtubule disorganization, we found that RO-3306
289 treatment resulted in uneven segregation of chromosomes into the two daughter cells (**Figure 8F,**
290 **8G**, upper). This effect of RO-3306 treatment was irrelevant to DNA synthesis since the total
291 chromosome area of both daughter cells was comparable between control and RO-3306-treated
292 cells (**Figure 8G**, upper left). The difference in chromosome area between the two daughter cells
293 was noticeably higher in the RO-3306-treated group compared to the control group (**Figure 8G**,
294 upper right). In Ki-67 knockdown cells, we also observed a similar phenotype in that Ki-67-
295 expressing cells exhibited uneven chromosome segregation (**Figure 8F, 8G**, lower panels). These
296 results support a role for CDK1 and Ki-67 in regulating microtubule and chromosome
297 organization.

298 Moreover, we analyzed the distribution of nuclear lipids after RO-3306 treatment. Similar
299 to the results of Ki-67 knockdown, the signal of nuclear lipids stained by DHPE-biotin was mostly
300 smeared around the chromosomal area, including intrachromosomal regions, after RO-3306
301 treatment (**Figure 9A**). RO-3306 impaired the perichromosomal distribution of nuclear lipids at
302 prometaphase (**Figure 9B**). The ratio of intra- to peri-chromosomal DHPE-biotin signals was also
303 increased by the RO-3306 treatment (**Figure 9C**). These results further support that the key cell
304 cycle regulator CDK1 regulates the distribution of nuclear lipids.

305

306 ## Discussion

307 Here, we have applied a super-resolution fluorescence imaging system, i.e., TT-ExM (Wang et al.,
308 2023, Hu et al., 2023), to reveal the dynamic distribution of nuclear lipids during the cell cycle,
309 showcasing the involvement of nuclear lipids in how Ki-67 acts in chromosome individualization
310 and segregation during mitosis. Our study provides three lines of evidence that Ki-67 regulates the

311 distribution of nuclear lipids on the outer surface and/or interior of condensed chromosomes. First,
312 although Ki-67 and nuclear lipids intermingle in the perichromosomal layer, our application of TT-
313 ExM super-resolution imaging enabled us to dissect the layer organization at the chromosomal
314 periphery, revealing that nuclear lipids or lipid-containing materials are enriched outside of Ki-67.
315 Therefore, Ki-67 may act as a barrier to prevent nuclear lipids from moving into chromosomal
316 interiors. Second, the enrichment of nuclear lipids at the chromosomal periphery is negatively
317 correlated with total protein and phosphorylation levels of Ki-67 during mitosis. Third, Ki-67
318 knockdown results in nuclear lipids invading the interior of mitotic chromosomes, confirming that
319 Ki-67 regulates the distribution of nuclear lipids during the cell cycle (**Figure 10**).

320 How does Ki-67 regulate the distribution of nuclear lipids at the periphery of condensed
321 chromosomes? It has been suggested previously that Ki-67 may serve as a surface-active agent
322 (surfactant) to mediate the individualization of sister chromatid pairs (Cuylen et al., 2016) and to
323 exclude the cytoplasm from fully condensed chromosomes (Cuylen-Haering et al., 2020).
324 Although the respective mechanisms remain unclear, it is reasonable to speculate that nuclear
325 lipids enriched at the chromosomal periphery likely cooperate with Ki-67 to facilitate the
326 individualization of sister chromatid pairs during mitosis. The general physicochemical features
327 of Ki-67 provide clues to the functional interplay between Ki-67 and nuclear lipids. Like many
328 surfactants, Ki-67 has an amphiphilic structure. The long N-terminal domain of Ki-67 is excluded
329 from chromatin, whereas its short C-terminal LR domain displays strong attraction to chromatin
330 (Cuylen et al., 2016). Moreover, the chromosome separation function of Ki-67 is not attributable
331 to a specific protein domain, but is correlated with the size and net charge of truncation mutants
332 that lack secondary structure (Cuylen et al., 2016). Thus, the amphiphilic molecular structure of
333 Ki-67 may disperse nuclear lipids or lipid-containing components via a liquid-liquid phase

334 transition mechanism, resulting in their accumulation at the chromosomal periphery. Consistent
335 with this supposition, our TT-ExM super-resolution imaging revealed that Ki-67 forms numerous
336 tiny granules on the surface of mitotic chromosomes, rather than presenting a smooth and
337 continuous thin layer. These tiny Ki-67-positive granules intermingle with lipid-containing nuclear
338 components on the outer surface of mitotic chromosomes (**Figure 3A, 4D**). We suggest that Ki-67
339 proteins and these lipid-containing components collectively form a perichromosomal layer that
340 mediates the individualization of sister chromatid pairs during mitosis.

341 In addition to forming a physical barrier via liquid-liquid phase separation (LLPS), CDK1-
342 mediated Ki-67 phosphorylation may also regulate the distribution of nuclear lipids. We found that
343 addition of the CDK1 inhibitor RO-3306 disrupted the organization of microtubules and
344 chromosomes and induced nuclear lipid invasion into intrachromosomal regions at prometaphase.
345 Heavy phosphorylation of Ki-67 may facilitate the formation of a negatively-charged barrier and
346 strengthen the effect of Ki-67 in preventing nuclear lipid invasion into the intrachromosomal
347 regions. However, since CDK1 phosphorylates many other proteins during mitosis (Petrone et al.,
348 2016, Lo Surdo et al., 2023), other CDK1 substrates may also contribute to regulating the
349 distribution of nuclear lipids. Nevertheless, our analyses using CDK1 inhibitors in the current
350 study support that the cell cycle controls nuclear lipid distributions (**Figure 10**).

351 Since the lipid-containing nuclear components also display amphiphilic characteristics, it
352 is also plausible that Ki-67 and the lipid-containing components may function redundantly, at least
353 partially, thereby explaining several interesting observations. First, Ki-67 is not an essential protein
354 but is a cell proliferation marker, with Ki-67 knockout cells still proliferating under cultured
355 conditions (Cuylen et al., 2016). Second, to date, Ki-67 homologs have only been detected in
356 vertebrates (Remnant et al., 2021). Proteins homologous to Ki-67 have not been identified or

357 characterized in any other non-vertebrate eukaryotes. Our results indicate that nuclear lipids exert
358 a novel role in isolating or individualizing condensed sister chromatid pairs during mitosis of
359 cultured mammalian cells. It would be interesting to investigate further if nuclear lipids in non-
360 vertebrate organisms also exhibit similar functions.

361 Our results are also consistent with previous reports (Prudovsky et al., 2012, Gould et al.,
362 2017) showing that PS is mainly present in epichromatin or on the outer surface of condensed
363 chromosomes during mitosis (**Figure 4**). Using biotin-DHPE, we show that nuclear lipids or lipid-
364 containing components accumulate around the periphery of entire chromosomes during mitosis
365 (**Figure 4**). Mammalian nuclei contain a variety of lipids, including PS, phosphatidylinositol,
366 cholesterol, free fatty acids, diacylglycerol, and sphingolipids (Ledeen and Wu, 2004). Further
367 investigations are needed to reveal if all these lipids or specific types of lipids are enriched around
368 the periphery of condensed chromosomes.

369 Lastly, our findings herein may provide a new perspective on mitosis in general. The NE,
370 which comprises two lipid bilayers, is a highly regulated membrane barrier that separates the
371 nucleus from the cytoplasm in eukaryotes. Depending on the organism and cell type, the NE
372 remains intact during closed mitosis or disassembles during open mitosis before chromosome
373 segregation. Closed mitosis occurs in many (but not all) fungi and is considered the most ancient
374 mechanism of eukaryotic cell division. In contrast, animals and plants undergo open mitosis, which
375 appears to have evolved independently several times (Cavalier-Smith, 2010). A few fungi (e.g.,
376 the fission yeast *Shizosaccharomyces japonicus* and the corn smut fungus *Ustilago maydis*)
377 undergo semi-open mitosis, in which the NE does not disassemble completely (Boettcher and
378 Barral, 2013). As yet, it is not fully understood why open mitosis prevails in animals and plants,
379 but not in fungi. The results from this study reveal that Ki-67 and nuclear lipids constitute a thin

380 “chromosome envelope” around each sister chromatid pair, with the transition from “nuclear
381 envelope” to “chromosome envelope” enabling continued isolation of genetic material from
382 cytoplasmic material, thereby ensuring the individualization of sister chromatid pairs, the
383 formation of star-like microtubule arrays, and proper chromosome segregation.
384

385 # Methods

386 **Antibodies and reagents**

387 Rabbit polyclonal HSP90 was a kind gift from Dr. Chung Wang (Institute of Molecular Biology,
388 Academia Sinica). Commercially available antibodies and chemicals used in this report are as
389 follows: rat monoclonal Ki-67 (SolA15, #14-569882, 1:2000 for immunoblotting, 1:500 for TT-
390 ExM, Invitrogen); rabbit polyclonal phospho-Ki-67 (301119, 1:500, Novocastra); mouse
391 monoclonal phosphatidylserine (PS) (1H6, 05-719, 1:200 for TT-ExM, Sigma-Aldrich); rabbit
392 polyclonal α-Tubulin (ab18251, 1:500, Abcam); chicken polyclonal GFP (ab13970, 1:1000 for TT-
393 ExM, Abcam); mouse monoclonal GFP (JL-8, 632381, 1:2000 for immunoblotting, Clontech);
394 Alexa Fluor-488-, 555- and 647-conjugated secondary antibodies (Invitrogen); Nocodazole
395 (M1404, Sigma-Aldrich); DAPI (D1306,1:1000, Invitrogen); PicoGreen (P11495, 1:1000,
396 ThermoFisher). Reagents used for DHPE TT-ExM are as follows: N-(Biotinoyl)-1,2-
397 dihexadecanoyl-snglycero-3-phosphoethanolamine, triethylammonium salt (Biotin-DHPE) (60022,
398 0.1mg/ml, Biotium); VECTASTAIN ABC-HRP Kit, peroxidase (standard), (PK-4000, Vector
399 Laboratory); Alexa fluor-555-conjugated tyramide (B40955, 1:100, Invitrogen); Amplification diluent
400 (FP1050, PerkinElmer); 6-((acryloyl)amino)hexanoic acid (Acryloyl-X, SE, A-20770,
401 ThermoFisher); Sodium acrylate (408220, Sigma-Aldrich); Acrylamide (A9099, Sigma-Aldrich);
402 N, N’-methylenebisacrylamide, (1551624, ThermoFisher); Ammonium persulfate, (APS, A9164,

403 Sigma-Aldrich); N,N,N,,N,-Tetramethylethylenediamine (TEMED, T7024, Sigma-Aldrich); 4-
404 Hydroxy-TEMPO (176141, Sigma-Aldrich); Sodium chloride (3624-69, J.T.Baker); Trypsin-
405 EDTA solution, 0.05% (25300-054, Gibco); RO-3306 (SML0569, Sigma-Aldrich); Methanol
406 (9093-68; J.T. Backer); Acetone (32201, Honeywell).
407
408 **Plasmid construction**
409 To generate the Ki67-miR knockdown constructs, an artificial miRNA was designed using
410 BLOCK-iT™ RNAi Designer (https://rnaidesigner.thermofisher.com/rnaiexpress/). According to
411 the ranking score, the top miRNA (nucleotide residues 3296-3319,
412 AAGAGCTTGCCTGATACAGAA) was chosen and cloned into pcDNA6.2-GW/EmGFP vector.
413 A control vector (pcDNA6.2–GW/EmGFP-miR, Invitrogen) expressing a scrambled miRNA (Hu
414 et al., 2020) predicted to not target any gene in mammalian genomes was used as the negative
415 control in our knockdown experiments.
416
417 **COS-7 culture and nocodazole treatment**
418 The monkey COS-7 fibroblast-like cell line (ATCC, CRL-1651) was maintained in DMEM
419 supplemented with 10% FBS, 1% penicillin/streptomycin and 2 mM glutamine. For mitotic cell cycle
420 analysis, cells were treated with 50 nM nocodazole for 6 h to synchronize the cell cycle in
421 prometaphase. Media were then washed out and the cells were allowed to recover for 15, 30, or 60
422 min to re-enter the mitotic cycle. Mitotic stages were identified based on chromosome patterning.
423 For the Ki-67 dephosphorylation experiment, we treated nocodazole-synchronized cells with 2 μM
424 of the CDK1 inhibitor, RO-3306, for 15 or 30 min after washing out nocodazole.
425
426 **Transfection and immunoblotting of COS-7 cells**

427 COS-7 cells were transfected with the indicated plasmids using PolyJet (SL100688, SignaGen
428 Laboratories) according to the manufacturer's instructions. For Ki-67 knockdown analysis, the
429 transfection period was extended to 2 days to enhance knockdown efficiency. For immunoblotting
430 analysis, cells were washed with PBS twice and lysed directly with SDS sample buffer. Total cell
431 lysates were separated by means of SDS-PAGE and analyzed by immunoblotting.
432
433 **Immunofluorescence analysis**
434 Regular immunostaining was performed as described previously (Hu et al., 2020). Briefly, cells
435 were washed with phosphate-buffered saline (PBS) and fixed with 4% paraformaldehyde (PFA)
436 and 4% sucrose in PBS for 10 min, followed by permeabilization with 0.2% Triton X-100 in PBS
437 for 15 min at room temperature. After blocking with 10% bovine serum albumin (BSA), the cells
438 were incubated with primary antibodies diluted in PBS containing 3% BSA and 0.1% horse serum
439 at 4 °C overnight. After washing with PBS several times, the cells were incubated with secondary
440 antibodies conjugated with Alexa Fluor-488, -555 or -647 (Invitrogen) and DNA dye for 2 h at
441 room temperature.
442
443 **Lipid staining**
444 Lipid labeling using biotin-DHPE (Wang et al., 2023) was performed before regular
445 immunostaining. After fixation with 4% paraformaldehyde (PFA) for 10 min, the cells were
446 washed with PBS and then treated with 0.1 mg/ml biotin-DHPE in 50% ethanol overnight at room
447 temperature. After washing with PBS several times, cells were further incubated with premixed
448 reagents A and B in the Vectastin ABC-HRP kit (Vector Laboratory) in TBS (1:50 dilution) for at
449 least 30 min. After washing with PBS, Alexa fluor-555-conjugated tyramide was diluted (1:50) in

450 amplification diluent and applied to the cells for 15 min. Following extensive washing, the biotin-
451 DHPE-stained cells were then deemed ready for regular immunostaining. To confirm that the
452 labeling of biotin-DHPE was lipid-dependent, 100% methanol or 100% acetone were added
453 separately into PFA-fixed cells for 10 min at 20 °C. Comparing the results from PFA fixation alone
454 with PFA followed by methanol or acetone treatment, we demonstrated lipid-specific staining by
455 biotin-DHPE.
456
457 **TT-ExM**
458 Immunostained COS-7 cells, prepared as described above, were subjected to TT-ExM (Wang et
459 al., 2023, Hu et al., 2023). After staining, the cells were washed with PBS three times and then
460 incubated with 0.1 mg/ml Acryloyl-X, SE in PBS overnight at 4 °C. After washing three times
461 with PBS, the coverslip with stained cells was placed on acrylamide solution (with the cell-
462 attached side facing down) at 37 °C for 2 h for gelation. After gelation was completed, the hydrogel
463 was immersed in trypsin digestion solution (0.05 % volume dilution: 2 μl trypsin-EDTA solution
464 in 4 ml low salt digestion buffer), and then incubated at room temperature for at least 20 h with
465 gently shaking. The digested hydrogel was transferred to a 10-cm dish filled with excess Milli-Q
466 water for free expansion for 2 h. The expanded samples were then imaged at room temperature
467 using an LSM980 laser scanning confocal microscope equipped with Airyscan 2 multiplex mode
468 SR-4Y. An LD LCI Plan-Apochromate 40X/1.2 Imm Corr DIC M27 objective was used for Z-
469 series image acquisition.
470
471 **Analyses of DHPE invasion, chromosomal layer patterning and chromosome area**

472 To quantify the immunoreactivities of DHPE signals in the intrachromosomal area, line scanning
473 was performed using the ImageJ/Fiji software. A 3 μm-wide line across the chromosome or
474 perichromosomal layer was drawn to quantify DHPE signals. The intersection of biotin-DHPE
475 signal and the chromosome boundary was set as a ratio of 1. The lowest ratio of biotin-DHPE was
476 identified as the lipid level in the intrachromosomal area. Ten individual chromosomes per cell
477 were quantified and averaged. For chromosomal layer analysis, post-expanded and LSM980-
478 acquired images were subjected to line scanning analysis across the perichromosomal layer. Line
479 histograms were used to exhibit the distribution pattern of pericromosomal components. Five
480 individual chromosomes per cell were quantified and averaged. For chromosome area analysis,
481 the area occupied by chromosomes was quantified based on DAPI signals using ImageJ/Fiji. For
482 chromosome segregation in anaphase, the total chromosome area and difference in area between
483 the two sister chromosomes were analyzed.
484
485 **Analysis of microtubule organization**
486 To analyze microtubule organization, cells were stained with α-tubulin to identify microtubule
487 filaments and then assessed by means of Sholl analysis (ImageJ/Fiji) (Chen et al., 2011, Hu et al.,
488 2020) to examine the extension pattern of tubule filaments and to count the numbers of
489 intersections. The total numbers of intersections and microtubule filament tips were counted to
490 represent microtubule organization. For the microtubule organization analysis, microtubules were
491 categorized into four types based on distribution patterns, i.e., organized, disorganized, two-star,
492 or extended. The percentage of each type was calculated to reveal the effect of RO-3306 on
493 microtubules during mitosis.
494

495 **Quantification and statistical analysis**

496 To avoid potential personal bias, all data were collected and analyzed blindly by having other lab
497 members relabel the samples. For each experiment, 10 cells were randomly collected from at least
498 two independent experiments for quantification. To analyze DHPE invasion into the chromosomal
499 area, line scanning analysis was performed at each mitotic stage using the ImageJ/FIJI software.
500 To analyze microtubule organization, Sholl analysis was performed in the ImageJ/FIJI software to
501 calculate numbers of microtubule filaments and their distribution patterns. Two-group
502 comparisons were analyzed with two-tailed unpaired Student's *t*-test. For more than two group
503 comparisons, a one-way analysis of variance (ANOVA) with Bonferroni's multiple comparison
504 post-hoc test was performed.

505

506 ## Declarations

507 **Ethics approval and consent to participate**

508 Not applicable.

509

510 **Consent for publication**

511 All authors have read and approved of its submission to this journal.

512

513 **Availability of data and materials**

514 All relevant data are within the paper and its Supporting information files. The file of
515 **Supplemental Table S1** contains the numerical data for all figures. **Supplemental Table S2**
516 contains all statistical results. **Supplemental Figure S1** contains uncropped blots of **Figure 5B**.

517

Competing interests

The authors declare no conflicts of interest.

Funding

Institute of Molecular Biology, Academia Sinica, Taiwan, Republic of China; and Academia Sinica, Taiwan, Republic of China [ASIA-111-L01 to Y.-P.H. and AS-TP-110-L10 to Y.-P.H. and B.-C.C.]; National Science and Technology Council, Taiwan, Republic of China [NSTC 110-2811-B-001-542 to TFW; NSTC 113-2320-B-001-015-MY3 and 113-2326-B-001-008 to Y.-P.H.].

Authors' contributions

Conceptualization: YPH, TFW; Funding acquisition: YPH, TFW; Investigation: HTH, UTTW, BCC, YPH; Methodology: HTH, UTTW, BCC, YPH, TFW; Project administration: YPH, TFW; Supervision: YPH, TFW; Visualization: HTH, YPH; Writing – original draft: HTH, YPH, TFW; Writing – review and editing: HTH, UTTW, BCC, YPH, TFW. All of the authors read and approved the manuscript.

Acknowledgements

We thank the Imaging Core Facility of the Institute of Molecular Biology, Academia Sinica, for technical support and John O′Brien for English editing.

Authors' information

Hsiao-Tang Hu: annebest999@gmail.com

Ueh-Ting Tim Wang: utwang.ee13@nycu.edu.tw

Bi-Chang Chen: chenb10@gate.sinica.edu.tw

Yi-Ping Hsueh: yph@gate.sinica.edu.tw

Ting-Fang Wang: tfwang@gate.sinica.edu.tw

References

ANDRÉS-SÁNCHEZ, N., FISHER, D. & KRASINSKA, L. 2022. Physiological functions and roles in cancer of the proliferation marker Ki-67. *J Cell Sci,* 135.

BOETTCHER, B. & BARRAL, Y. 2013. The cell biology of open and closed mitosis. *Nucleus,* 4**,** 160-5.

BOOTH, D. G. & EARNSHAW, W. C. 2017. Ki-67 and the Chromosome Periphery Compartment in Mitosis. *Trends Cell Biol,* 27**,** 906-916.

BOOTH, D. G., TAKAGI, M., SANCHEZ-PULIDO, L., PETFALSKI, E., VARGIU, G., SAMEJIMA, K., IMAMOTO, N., PONTING, C. P., TOLLERVEY, D., EARNSHAW, W. C. & VAGNARELLI, P. 2014. Ki-67 is a PP1-interacting protein that organises the mitotic chromosome periphery. *eLife,* 3**,** e01641.

CAVALIER-SMITH, T. 2010. Origin of the cell nucleus, mitosis and sex: roles of intracellular coevolution. *Biol Direct,* 5**,** 7.

CERMELLI, S., GUO, Y., GROSS, S. P. & WELTE, M. A. 2006. The lipid-droplet proteome reveals that droplets are a protein-storage depot. *Curr Biol,* 16**,** 1783-95.

CHANG, J. B., CHEN, F., YOON, Y. G., JUNG, E. E., BABCOCK, H., KANG, J. S., ASANO, S., SUK, H. J., PAK, N., TILLBERG, P. W., WASSIE, A. T., CAI, D. & BOYDEN, E. S. 2017. Iterative expansion microscopy. *Nat Methods,* 14**,** 593-599.

CHEN, C. Y., LIN, C. W., CHANG, C. Y., JIANG, S. T. & HSUEH, Y. P. 2011. Sarm1, a negative regulator of innate immunity, interacts with syndecan-2 and regulates neuronal morphology. *J Cell Biol,* 193**,** 769-84.

CHEN, F., TILLBERG, P. W. & BOYDEN, E. S. 2015. Optical imaging. Expansion microscopy. *Science,* 347**,** 543-8.

CUYLEN, S., BLAUKOPF, C., POLITI, A. Z., MÜLLER-REICHERT, T., NEUMANN, B., POSER, I., ELLENBERG, J., HYMAN, A. A. & GERLICH, D. W. 2016. Ki-67 acts as a biological surfactant to disperse mitotic chromosomes. *Nature,* 535**,** 308-12.

CUYLEN-HAERING, S., PETROVIC, M., HERNANDEZ-ARMENDARIZ, A., SCHNEIDER, M. W. G., SAMWER, M., BLAUKOPF, C., HOLT, L. J. & GERLICH, D. W. 2020. Chromosome clustering by Ki-67 excludes cytoplasm during nuclear assembly. *Nature,* 587**,** 285-290.

DIDONATO, D. & BRASAEMLE, D. L. 2003. Fixation Methods for the Study of Lipid Droplets by Immunofluorescence Microscopy. *Journal of Histochemistry & Cytochemistry,* 51**,** 773-780.

DIRIL, M. K., RATNACARAM, C. K., PADMAKUMAR, V. C., DU, T., WASSER, M., COPPOLA, V., TESSAROLLO, L. & KALDIS, P. 2012. Cyclin-dependent kinase 1 (Cdk1) is essential for cell division and suppression of DNA re-replication but not for liver regeneration. *Proceedings of the National Academy of Sciences,* 109**,** 3826-3831.

FUJIMOTO, T. 2022. Nuclear lipid droplets - how are they different from their cytoplasmic siblings? *J Cell Sci,* 135.

GARCIA-GIL, M. & ALBI, E. 2017. Nuclear Lipids in the Nervous System: What they do in Health and Disease. *Neurochem Res,* 42**,** 321-336.

GARWAIN, O., SUN, X., IYER, D. R., LI, R., ZHU, L. J. & KAUFMAN, P. D. 2021. The chromatin-binding domain of Ki-67 together with p53 protects human chromosomes from mitotic damage. *Proceedings of the National Academy of Sciences,* 118**,** e2021998118.

GAUTIER, T., MASSON, C., QUINTANA, C., ARNOULT, J. & HERNANDEZ-VERDUN, D. 1992. The ultrastructure of the chromosome periphery in human cell lines. An in situ study using cryomethods in electron microscopy. *Chromosoma,* 101**,** 502-10.

GOULD, T. J., TÓTH, K., MÜCKE, N., LANGOWSKI, J., HAKUSUI, A. S., OLINS, A. L. & OLINS, D. E. 2017. Defining the epichromatin epitope. *Nucleus,* 8**,** 625-640.

GUILLEN-CHABLE, F., BAYONA, A., RODRÍGUEZ-ZAPATA, L. C. & CASTANO, E. 2021. Phase Separation of Intrinsically Disordered Nucleolar Proteins Relate to Localization and Function. *Int J Mol Sci,* 22.

HERNANDEZ-ARMENDARIZ, A., SORICHETTI, V., HAYASHI, Y., KOSKOVA, Z., BRUNNER, A., ELLENBERG, J., ŠARIĆ, A. & CUYLEN-HAERING, S. 2024. A liquid-like coat mediates chromosome clustering during mitotic exit. *Mol Cell,* 84**,** 3254-3270.e9.

HSU, T. C., ARRIGHI, F. E., KLEVECZ, R. R. & BRINKLEY, B. R. 1965. The nucleoli in mitotic divisions of mammalian cells in vitro. *J Cell Biol,* 26**,** 539-53.

HU, H. T., HUANG, T. N. & HSUEH, Y. P. 2020. KLHL17/Actinfilin, a brain-specific gene associated with infantile spasms and autism, regulates dendritic spine enlargement. *J Biomed Sci,* 27**,** 103.

HU, H. T., LIN, Y. J., WANG, U. T., LEE, S. P., LIOU, Y. H., CHEN, B. C. & HSUEH, Y. P. 2023. Autism-related KLHL17 and SYNPO act in concert to control activity-dependent dendritic spine enlargement and the spine apparatus. *PLoS Biol,* 21**,** e3002274.

KILL, I. R. 1996. Localisation of the Ki-67 antigen within the nucleolus. Evidence for a fibrillarin-deficient region of the dense fibrillar component. *J Cell Sci,* 109 (Pt 6)**,** 1253-63.

KUMANSKI, S., VIART, B. T., KOSSIDA, S. & MORIEL-CARRETERO, M. 2021. Lipid Droplets Are a Physiological Nucleoporin Reservoir. *Cells,* 10.

LEDEEN, R. W. & WU, G. 2004. Nuclear lipids: key signaling effectors in the nervous system and other tissues1. *Journal of Lipid Research,* 45**,** 1-8.

LEDEEN, R. W. & WU, G. 2008. Nuclear sphingolipids: metabolism and signaling. *J Lipid Res,* 49**,** 1176-86.

LO SURDO, P., IANNUCCELLI, M., CONTINO, S., CASTAGNOLI, L., LICATA, L., CESARENI, G. & PERFETTO, L. 2023. SIGNOR 3.0, the SIGnaling network open resource 3.0: 2022 update. *Nucleic Acids Res,* 51**,** D631-d637.

LOUVEL, V., HAASE, R., MERCEY, O., LAPORTE, M. H., ELOY, T., BAUDRIER, É., FORTUN, D., SOLDATI-FAVRE, D., HAMEL, V. & GUICHARD, P. 2023. iU-ExM: nanoscopy of organelles and tissues with iterative ultrastructure expansion microscopy. *Nat Commun,* 14**,** 7893.

M'SAAD, O. & BEWERSDORF, J. 2020. Light microscopy of proteins in their ultrastructural context. *Nat Commun,* 11**,** 3850.

MA, K., LUO, M., XIE, G., WANG, X., LI, Q., GAO, L., YU, H. & YU, X. 2022. Ribosomal RNA regulates chromosome clustering during mitosis. *Cell Discovery,* 8**,** 51.

MA, N., MATSUNAGA, S., TAKATA, H., ONO-MANIWA, R., UCHIYAMA, S. & FUKUI, K. 2007. Nucleolin functions in nucleolus formation and chromosome congression. *J Cell Sci,* 120**,** 2091-105.

MASSACCI, G., PERFETTO, L. & SACCO, F. 2023. The Cyclin-dependent kinase 1: more than a cell cycle regulator. *British Journal of Cancer,* 129**,** 1707-1716.

MCDONNELL, E., CROWN, S. B., FOX, D. B., KITIR, B., ILKAYEVA, O. R., OLSEN, C. A., GRIMSRUD, P. A. & HIRSCHEY, M. D. 2016. Lipids Reprogram Metabolism to Become a Major Carbon Source for Histone Acetylation. *Cell Rep,* 17**,** 1463-1472.

634 MORIEL-CARRETERO, M. 2021. The Many Faces of Lipids in Genome Stability (and How to
635 Unmask Them). *Int J Mol Sci,* 22.
636 MOROVICZ, A. P., MAZLOUMI GAVGANI, F., JACOBSEN, R. G., SKUSETH SLINNING,
637 M., TURCU, D. C. & LEWIS, A. E. 2022. Phosphoinositide 3-kinase signalling in the nucleolus.
638 *Adv Biol Regul,* 83**,** 100843.
639 MORTIER, E., WUYTENS, G., LEENAERTS, I., HANNES, F., HEUNG, M. Y., DEGEEST, G.,
640 DAVID, G. & ZIMMERMANN, P. 2005. Nuclear speckles and nucleoli targeting by PIP2-PDZ
641 domain interactions. *Embo j,* 24**,** 2556-65.
642 MOYNE, G. & GARRIDO, J. 1976. Ultrastructural evidence of mitotic perichromosomal
643 ribonucleoproteins in hamster cells. *Exp Cell Res,* 98**,** 237-47.
644 OSBORNE, S. L., THOMAS, C. L., GSCHMEISSNER, S. & SCHIAVO, G. 2001. Nuclear
645 PtdIns(4,5)P2 assembles in a mitotically regulated particle involved in pre-mRNA splicing. *J*
646 *Cell Sci,* 114**,** 2501-11.
647 PAYRASTRE, B., NIEVERS, M., BOONSTRA, J., BRETON, M., VERKLEIJ, A. J. & VAN
648 BERGEN EN HENEGOUWEN, P. M. 1992. A differential location of phosphoinositide kinases,
649 diacylglycerol kinase, and phospholipase C in the nuclear matrix. *J Biol Chem,* 267**,** 5078-84.
650 PETRONE, A., ADAMO, M. E., CHENG, C. & KETTENBACH, A. N. 2016. Identification of
651 Candidate Cyclin-dependent kinase 1 (Cdk1) Substrates in Mitosis by Quantitative
652 Phosphoproteomics. *Mol Cell Proteomics,* 15**,** 2448-61.
653 PRUDOVSKY, I., VARY, C. P., MARKAKI, Y., OLINS, A. L. & OLINS, D. E. 2012.
654 Phosphatidylserine colocalizes with epichromatin in interphase nuclei and mitotic
655 chromosomes. *Nucleus,* 3**,** 200-10.
656 REMNANT, L., KOCHANOVA, N. Y., REID, C., CISNEROS-SOBERANIS, F. & EARNSHAW,
657 W. C. 2021. The intrinsically disorderly story of Ki-67. *Open Biol,* 11**,** 210120.
658 ROMANAUSKA, A. & KÖHLER, A. 2018. The Inner Nuclear Membrane Is a Metabolically
659 Active Territory that Generates Nuclear Lipid Droplets. *Cell,* 174**,** 700-715.e18.
660 SAIWAKI, T., KOTERA, I., SASAKI, M., TAKAGI, M. & YONEDA, Y. 2005. In vivo dynamics
661 and kinetics of pKi-67: transition from a mobile to an immobile form at the onset of anaphase.
662 *Exp Cell Res,* 308**,** 123-34.
663 SHOLL, D. A. 1953. Dendritic organization in the neurons of the visual and motor cortices of the
664 cat. *J Anat,* 87**,** 387-406.
665 STAMATIOU, K., HUGUET, F., SERAPINAS, L. V., SPANOS, C., RAPPSILBER, J. &
666 VAGNARELLI, P. 2024. Ki-67 is necessary during DNA replication for fork protection and
667 genome stability. *Genome Biology,* 25**,** 105.
668 STAMATIOU, K. & VAGNARELLI, P. 2021. Chromosome clustering in mitosis by the nuclear
669 protein Ki-67. *Biochem Soc Trans,* 49**,** 2767-2776.
670 SUN, X. & KAUFMAN, P. D. 2018. Ki-67: more than a proliferation marker. *Chromosoma,* 127**,**
671 175-186.
672 TAKAGI, M., NISHIYAMA, Y., TAGUCHI, A. & IMAMOTO, N. 2014. Ki67 antigen contributes
673 to the timely accumulation of protein phosphatase 1γ on anaphase chromosomes. *J Biol Chem,*
674 289**,** 22877-22887.
675 TAKAGI, M., ONO, T., NATSUME, T., SAKAMOTO, C., NAKAO, M., SAITOH, N.,
676 KANEMAKI, M. T., HIRANO, T. & IMAMOTO, N. 2018. Ki-67 and condensins support the
677 integrity of mitotic chromosomes through distinct mechanisms. *Journal of Cell Science,* 131.

678 VANN, L. R., WOODING, F. B., IRVINE, R. F. & DIVECHA, N. 1997. Metabolism and possible
679 compartmentalization of inositol lipids in isolated rat-liver nuclei. *Biochem J,* 327 (Pt 2)**,** 569-
680 76.
681 VORE, M., LU, A. Y. H., KUNTZMAN, R. & CONNEY, A. H. 1974. Organic Solvent Extraction
682 of Liver Microsomal Lipid. *Molecular Pharmacology,* 10**,** 963.
683 WANG, U.-T. T., TIAN, X., LIOU, Y.-H., LEE, S.-P., HU, H.-T., LU, C.-H., LIN, P.-T., CHENG,
684 Y.-J., CHEN, P. & CHEN, B.-C. 2023. Protein and lipid expansion microscopy with trypsin and
685 tyramide signal amplification for 3D imaging. *Scientific Reports,* 13**,** 21922.
686 WANG, Y.-H., HARIHARAN, A., BASTIANELLO, G., TOYAMA, Y., SHIVASHANKAR, G. V.,
687 FOIANI, M. & SHEETZ, M. P. 2017. DNA damage causes rapid accumulation of
688 phosphoinositides for ATR signaling. *Nature Communications,* 8**,** 2118.
689 WASSIE, A. T., ZHAO, Y. & BOYDEN, E. S. 2019. Expansion microscopy: principles and uses
690 in biological research. *Nat Methods,* 16**,** 33-41.
691 YAMAZAKI, H., TAKAGI, M., KOSAKO, H., HIRANO, T. & YOSHIMURA, S. H. 2022. Cell
692 cycle-specific phase separation regulated by protein charge blockiness. *Nature Cell Biology,* 24**,**
693 625-632.
694 YILDIRIM, S., CASTANO, E., SOBOL, M., PHILIMONENKO, V. V., DZIJAK, R., VENIT, T.
695 & HOZÁK, P. 2013. Involvement of phosphatidylinositol 4,5-bisphosphate in RNA polymerase
696 I transcription. *J Cell Sci,* 126**,** 2730-9.
697 ZHANG, X. H., ZHAO, C. & MA, Z. A. 2007. The increase of cell-membranous
698 phosphatidylcholines containing polyunsaturated fatty acid residues induces phosphorylation
699 of p53 through activation of ATR. *J Cell Sci,* 120**,** 4134-43.
700 ZOU, C., ELLIS, B. M., SMITH, R. M., CHEN, B. B., ZHAO, Y. & MALLAMPALLI, R. K. 2011.
701 Acyl-CoA:lysophosphatidylcholine acyltransferase I (Lpcat1) catalyzes histone protein O-
702 palmitoylation to regulate mRNA synthesis. *J Biol Chem,* 286**,** 28019-25.
703

Figures and Figure Legends

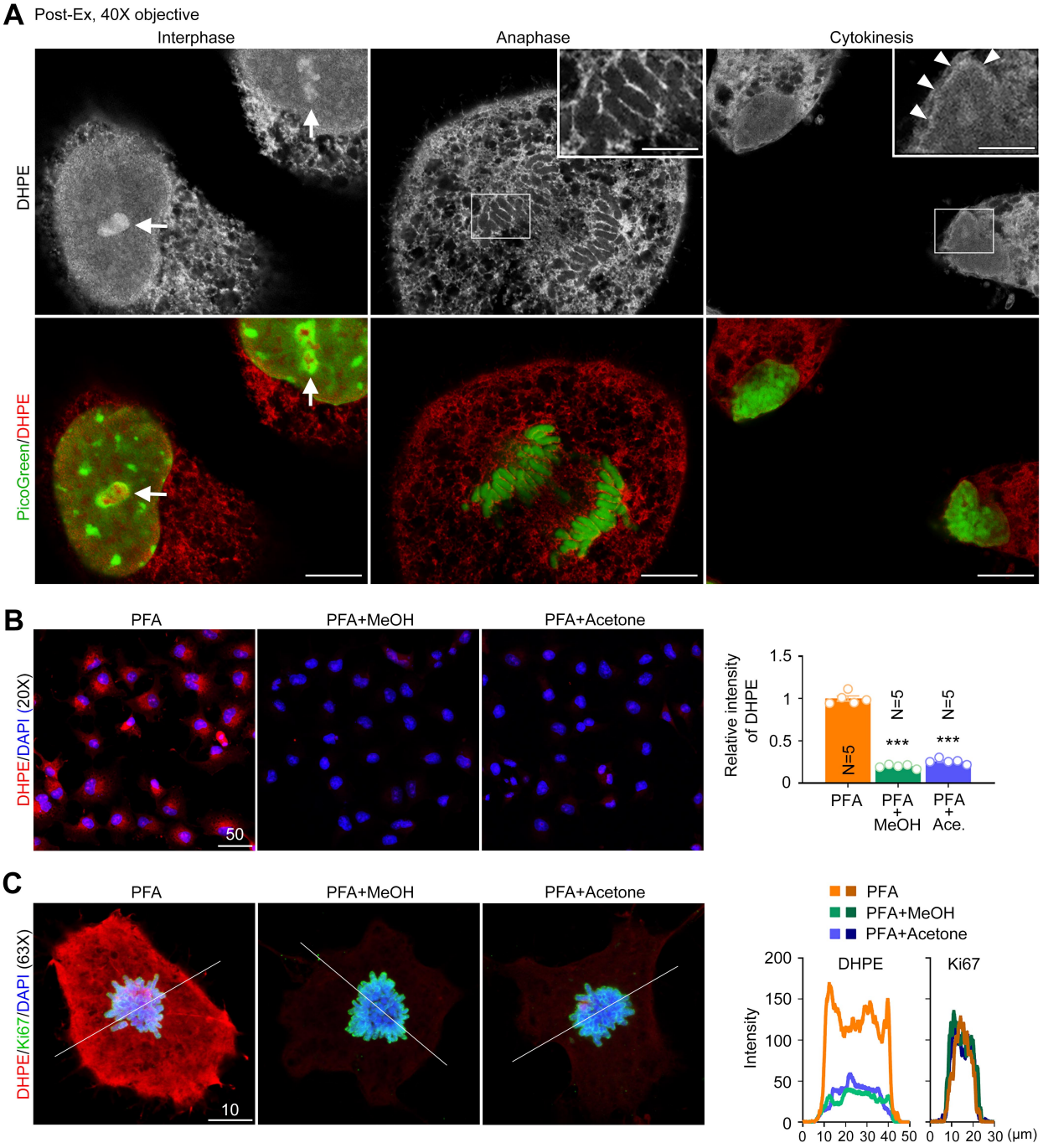

Figure 1. TT-ExM reveals the distribution of lipids and DNA throughout the cell cycle. (**A**) COS-7 cells were stained with biotin-DHPE and PicoGreen and subjected to TT-ExM. Images were acquired using an LSM700 confocal microscope. Different stages of the cell cycle are shown. Arrows indicate the biotin-DHPE signals located in the nucleolus during interphase. The enlarged chromosome segment shows the enriched biotin-DHPE signals at the perichromosomal layers

711 during anaphase. Arrowheads indicate the reforming nuclear envelope after telophase. (**B**)
712 Methanol or acetone treatments reduce biotin-DHPE signals. Left: Representative images. Right:
713 quantification of biotin-DHPE signals. (**C**) Higher magnification images show the effect of
714 methanol or acetone on lipids, but neither treatment affects the signals of Ki-67 or chromosomal
715 DNA. The fine white lines indicate the location of the line scan for quantification shown on the
716 right. Scale bars: (**A**) whole cells: 20 μm; enlarged segment: 8 μm. (**B**) Upper: 50 μm; lower: 10
717 μm.
718

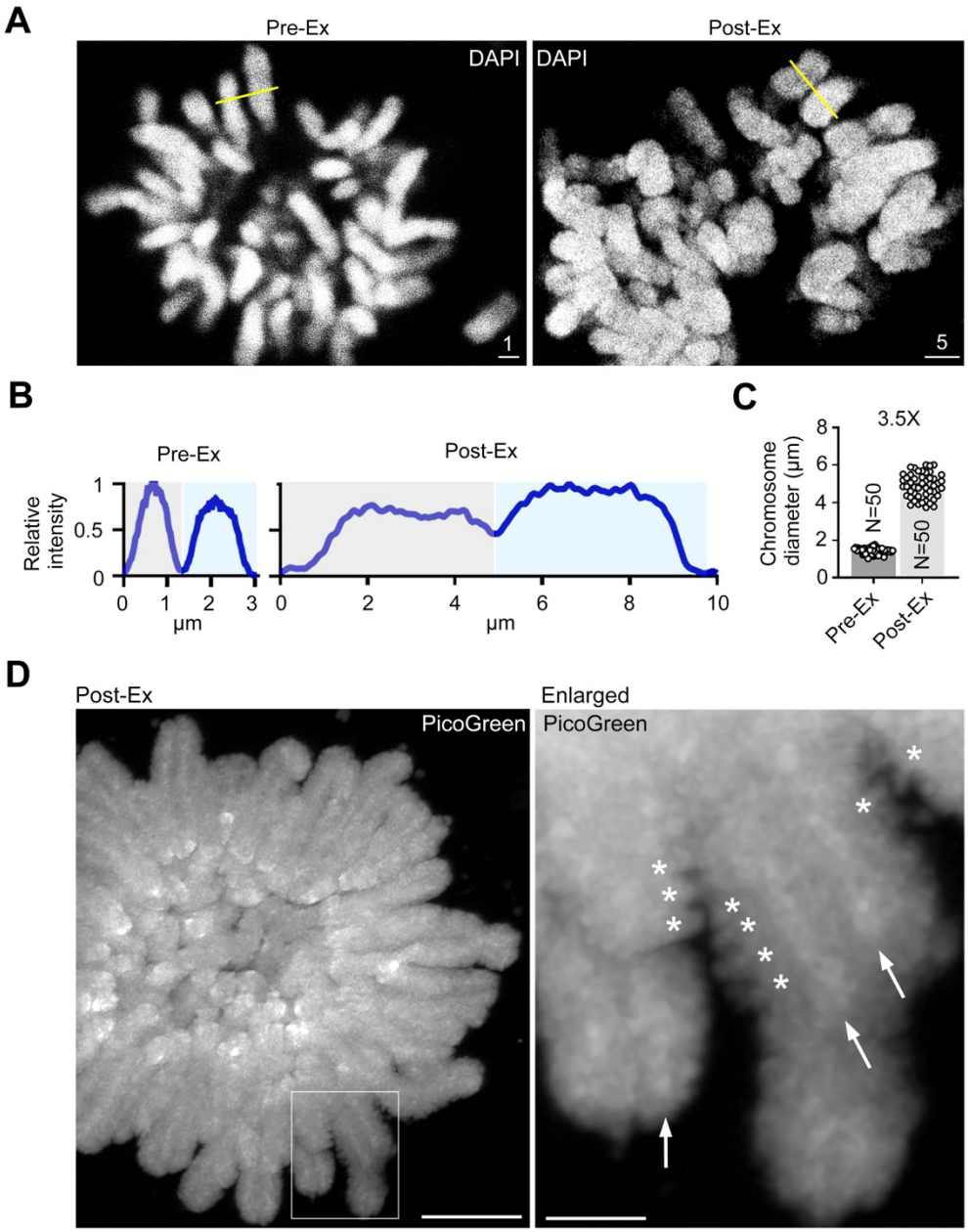

Figure 2. Chromosomal DNA expands isotropically in prometaphase.

COS-7 cells were subjected to TT-ExM using PicoGreen or DAPI for DNA staining. Images were acquired using an LSM980 confocal microscope with an Airyscan2 detector. (**A**) Representative images of mitotic chromosomes in prometaphase before and after expansion. Yellow lines are examples of the perpendicular line drawn for line scanning analysis. (**B**)-(**C**) Quantification of chromosome diameters in Pre-Ex and Post-Ex cells. Light grey and blue blocks indicate the regions of two adjacent chromosomes for measurement. Expansion was determined to be 3.5-fold. (**D**) Confocal images of PicoGreen signals in entire Post-Ex cells and enlarged chromosome segments.

728 PicoGreen signal revealed likely chromosome axes displaying a denser DNA signal (arrows), as
729 well as chromosomal loops (asterisks). Scale bars: (**A**) pre-Ex: 1 µm; post-Ex: 5 µm; (**B**) whole
730 cells: 10 µm; enlarged segment: 2.5 µm.
731

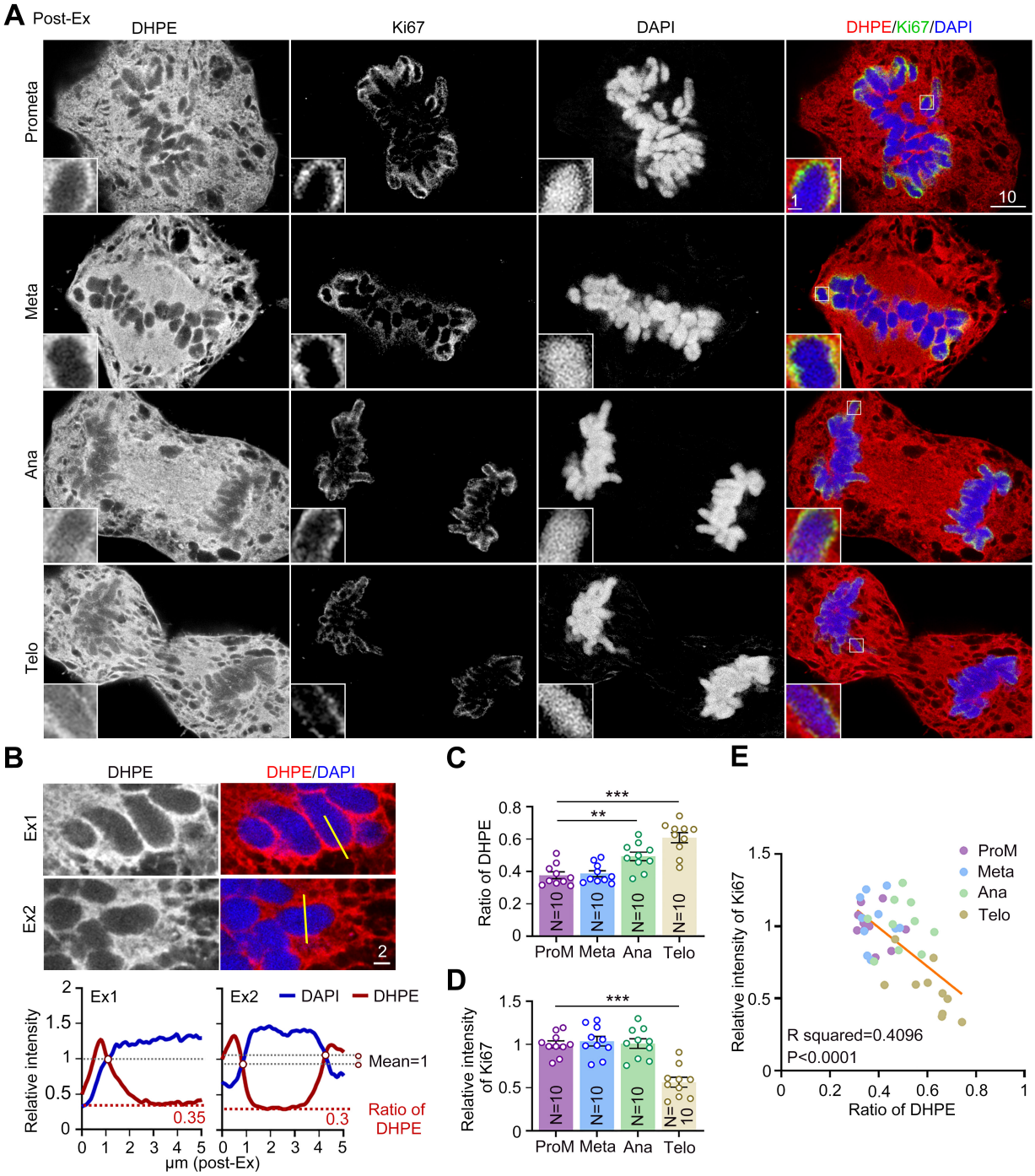

Figure 3. Distribution patterns of Ki-67 and biotin-DHPE signals during mitosis. COS-7 cells were subjected to TT-ExM and stained using biotin-DHPE, Ki-67 antibody and DAPI. Images at different mitotic stages were acquired using an LSM980 confocal microscope with Airyscan2. (**A**) Confocal images of entire cells and enlarged chromosome segments at different stages of mitosis: Prometa (prometaphase); Meta (metaphase); Ana (anaphase); Telo (telophase). The original regions of the enlarged images are indicated only in the rightmost panels. (**B**) Line

739 scanning analysis of biotin-DHPE distribution across the perichromosomal layer and chromosome.
740 Yellow lines indicate the regions analyzed in the two examples, Ex1 and Ex2. Lower panel: The
741 results of line scanning analysis on Ex1 and Ex2. The red open circles indicate the intersection of
742 biotin-DHPE signal and the chromosome boundary, which was set as a ratio of 1. The lowest ratio
743 of biotin-DHPE was identified as the relative lipid level in the chromosome interior. (**C**) Ratio of
744 the biotin-DHPE signal in the intrachromosomal area to that at the periphery. The ratio was lower
745 in prometaphase and metaphase, but increased in anaphase and telophase. (**D**) Relative levels of
746 total Ki-67 immunoreactivity, which clearly declined during telophase. (**E**) Negative correlation
747 of the biotin-DHPE ratio and Ki-67 signal intensity. The sample size "N" indicates the number of
748 examined cells. The data represent mean ± SEM and individual data points are also shown. All
749 data were collected from at least two independent experiments. ** $P < 0.01$; *** $P < 0.001$; one-
750 way ANOVA. Scale bars: (**A**) whole cells: 10 μm; enlarged segment: 1 μm; (**B**) 2 μm.
751

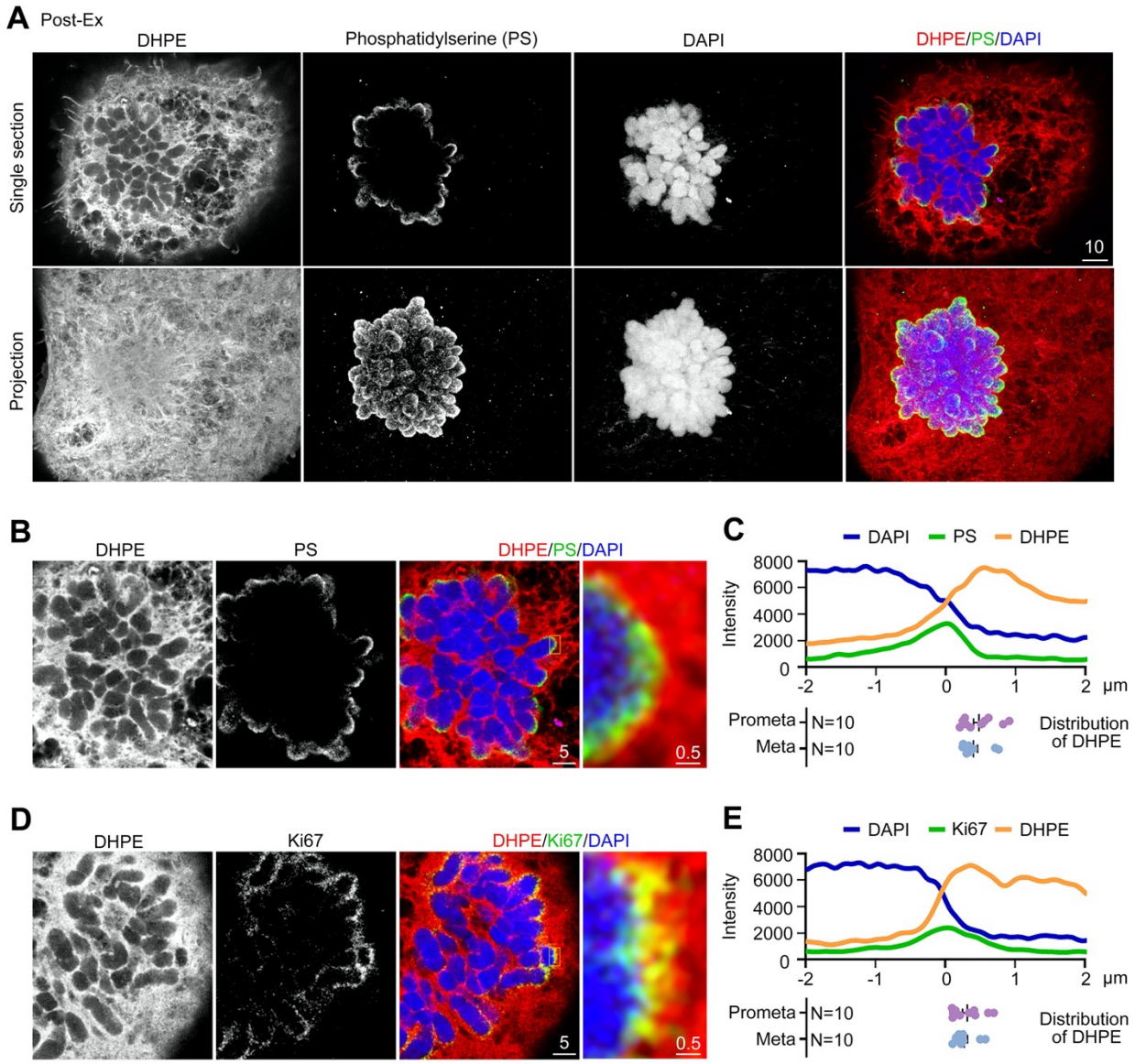

Figure 4. Relative distribution patterns of Ki-67, biotin-DHPE and PS.

COS-7 cells were subjected to TT-ExM and stained using antibodies recognizing Ki-67 and phosphatidylserine (PS), as well as for biotin-DHPE and DAPI. Images of cells in prometaphase and metaphase were acquired using an LSM980 microscope with an AiryScan2 detector. (**A**) Confocal images of lipid components (biotin-DHPE and PS) during prometaphase. Upper: Single section. Lower: Z-projection. Biotin-DHPE was distributed throughout cells and covered the entire chromosomes. PS was only located in regions of epichromatin. (**B**)-(**C**) Distribution of biotin-DHPE and PS. (**D**)-(**E**) Distribution of biotin-DHPE and Ki-67. (**B**), (**D**) Representative confocal images. The 10X enlarged images of the insets at regions of epichromatin in the whole-cell images are shown in the rightmost panels. (**C**), (**E**) The results of line scanning. Upper: an example of the

763 line scanning result. Lower: the relative positions of the peaks of biotin-DHPE signals. The peaks
764 of PS and Ki-67 signals at the chromosome edge are set as 0. Biotin-DHPE signals are always
765 present at the outer part of perichromosomal layer relative to the PS and Ki-67 signals. The sample
766 size "N" indicates the number of examined cells in prometaphase and metaphase. Scale bars: (**A**)
767 10 μm; (**B**), (**D**) whole cells: 5 μm; enlarged segment: 0.5 μm.
768

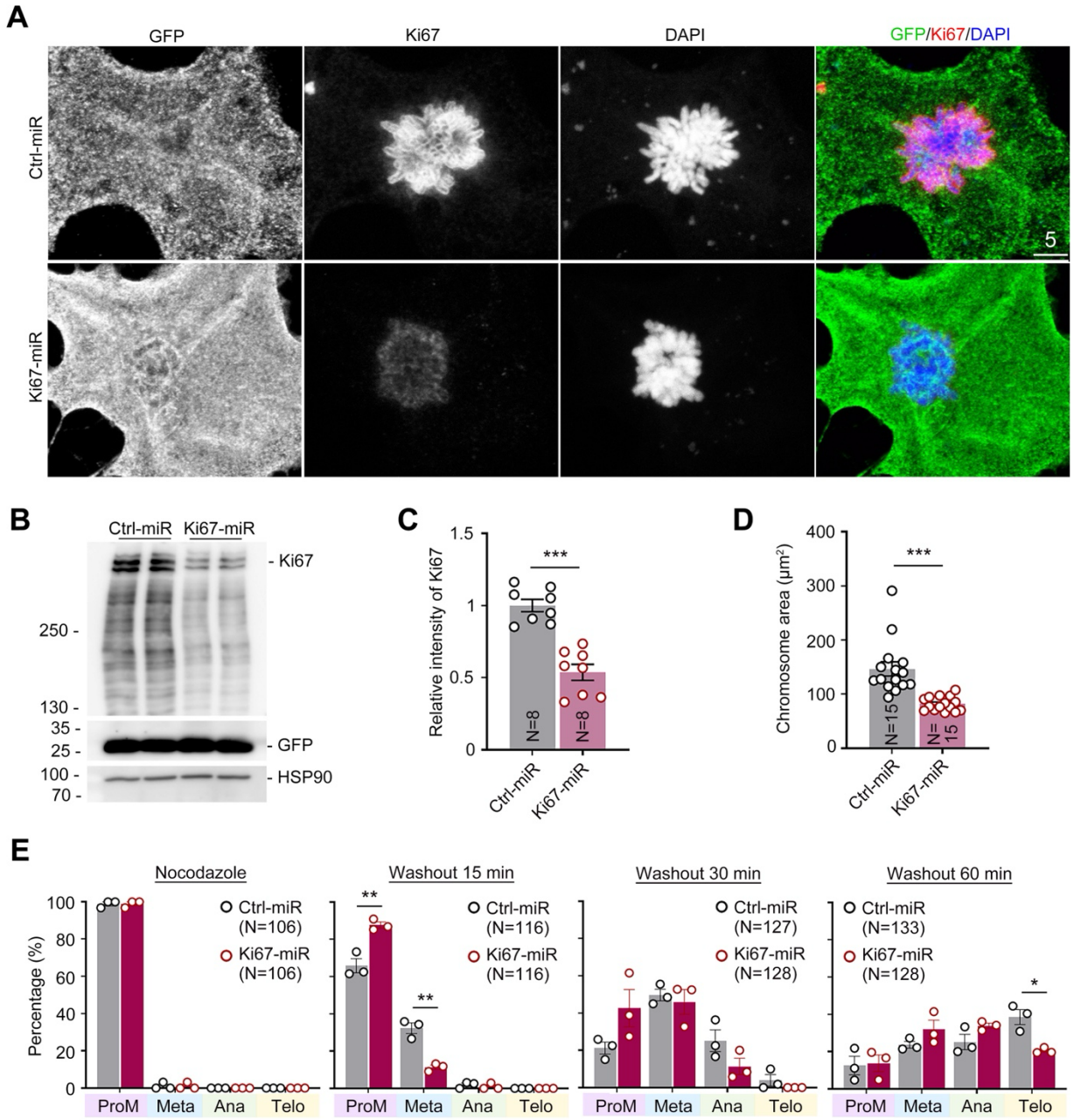

Figure 5. Ki-67 knockdown alters chromosome structure and delays mitotic progress. COS-7 cells were transfected with Ki67-miR or Ctrl-miR and then stained with Ki-67 antibody and DAPI. Since miR constructs coexpress GFP, GFP signals were used to label transfected cells. Images were acquired using an LSM700 confocal microscope. (**A**) Representative confocal images in prometaphase. Ki-67 signal intensity (**C**) and chromosome areas (**D**) were analyzed for transfected cells. (**B**) The knockdown effect of Ki67-miR. Whole-cell extracts were collected and immunoblotted with Ki-67 antibody to detect endogenous Ki-67 protein levels. GFP and HSP90

are loading controls. (**C**) The relative Ki-67 signals in Ki67-miR- and Ctrl-miR-expressing cells. (**D**) Loss of Ki-67 reduces chromosome area. (**E**) Ki-67 knockdown delays progress of mitosis. Cells were treated with 50 nM nocodazole for 6 h to synchronize the cell cycle at prometaphase. After removing nocodazole, the cells were allowed to recover for 15, 30 or 60 mins before being harvested for immunostaining. Mitotic stages were determined according to chromosome patterning. The sample sizes (N) of independent preparations (**C**) or examined cells (**D**, **E**) are indicated in the panels. In (**E**), total cell numbers were collected from three independent experiments. The data represent mean ± SEM and individual data points are also shown. All data were collected from at least two independent experiments. * $P < 0.05$; ** $P < 0.01$; *** $P < 0.001$; two-tailed unpaired Student's *t*-test. Scale bars: (**A**) 5 μm.

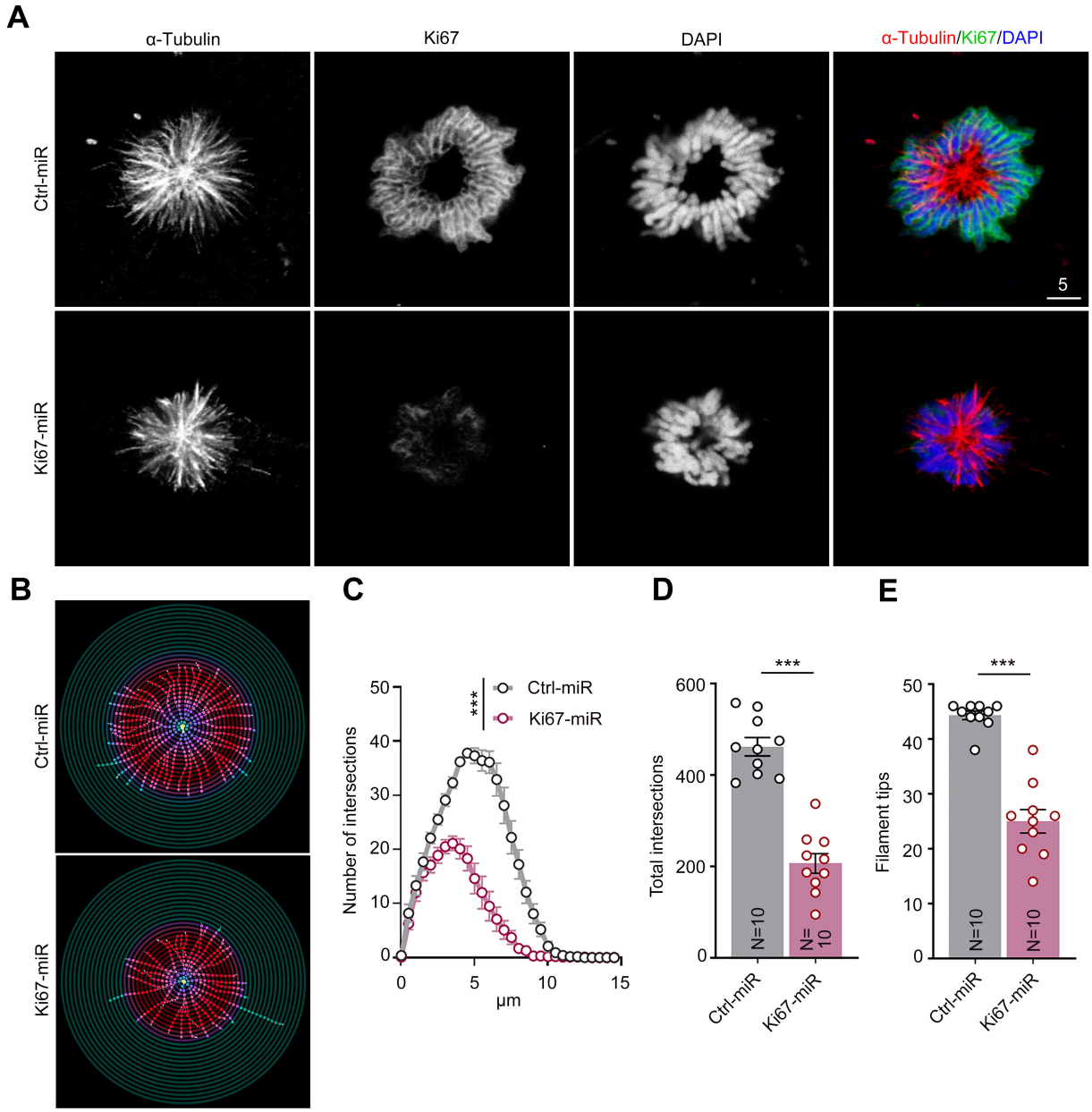

Figure 6. Loss of Ki-67 disturbs microtubule organization.

COS-7 cells were transfected with Ki67-miR or Ctrl-miR plasmids and stained with Ki-67 and α-tubulin (for microtubule) antibodies and DAPI. Images were acquired using an LSM700 confocal microscope. (**A**) Confocal images of microtubule filaments during prometaphase. Representative images of Crtl-miR- and Ki67-miR-expressing cells are shown. (**B**)-(**E**) Quantification of microtubule organization by Sholl analysis. (**B**) Representative images of Sholl analysis. (**C**) The distribution of numbers of intersections. (**D**) Total numbers of intersections. (**E**) Total numbers of microtubule filament tips. The sample size "N" indicates the number of examined cells. The data

797 represent mean ± SEM and individual data points are also shown. All data were collected from
798 two independent experiments. *** $P < 0.001$; two-tailed unpaired Student's *t*-test. Scale bars: **(A)**
799 5 μm.
800

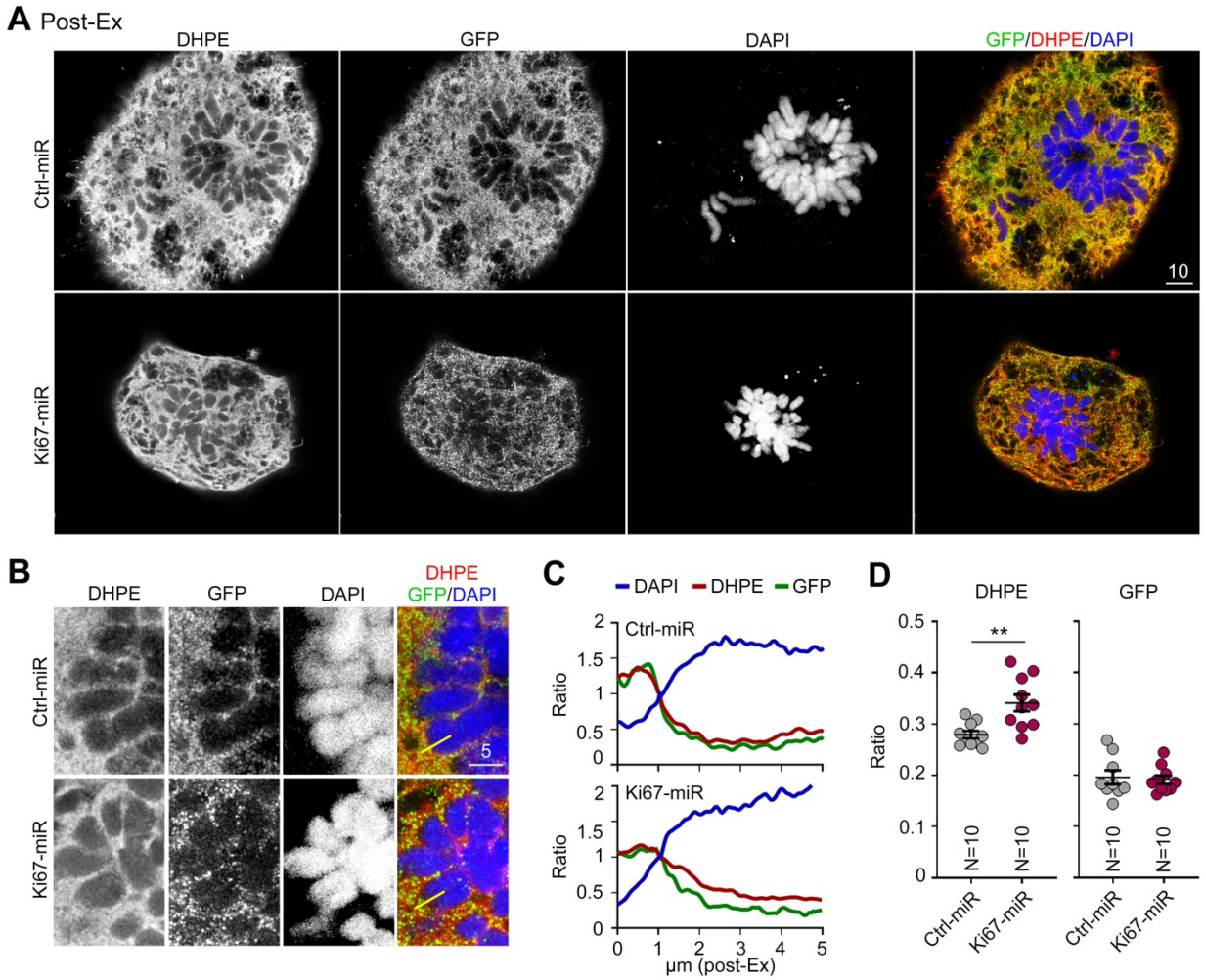

Figure 7. Lipid distribution is altered by Ki-67 knockdown.

COS-7 cells were transfected with Ki67-miR or Ctrl-miR plasmids and then stained with biotin-DHPE, Ki-67 antibody and DAPI for TT-ExM. An LSM980 microscope with an AiryScan2 detector was used to acquire images of the cells in prometaphase. (**A**) Representative confocal images. (**B**)-(**D**) Line scanning analysis reveals a change in biotin-DHPE distribution. The yellow lines indicate the regions subjected to line scanning. GFP serves as a control that is insensitive to Ki-67 knockdown. The sample size "N" indicates the number of examined cells. The data represent mean ± SEM and individual data points are also shown. All data were collected from at least two dependent experiments. ** $P < 0.01$; two-tailed unpaired Student's *t*-test. Scale bars: (**A**) 10 μm; (**B**) 5 μm.

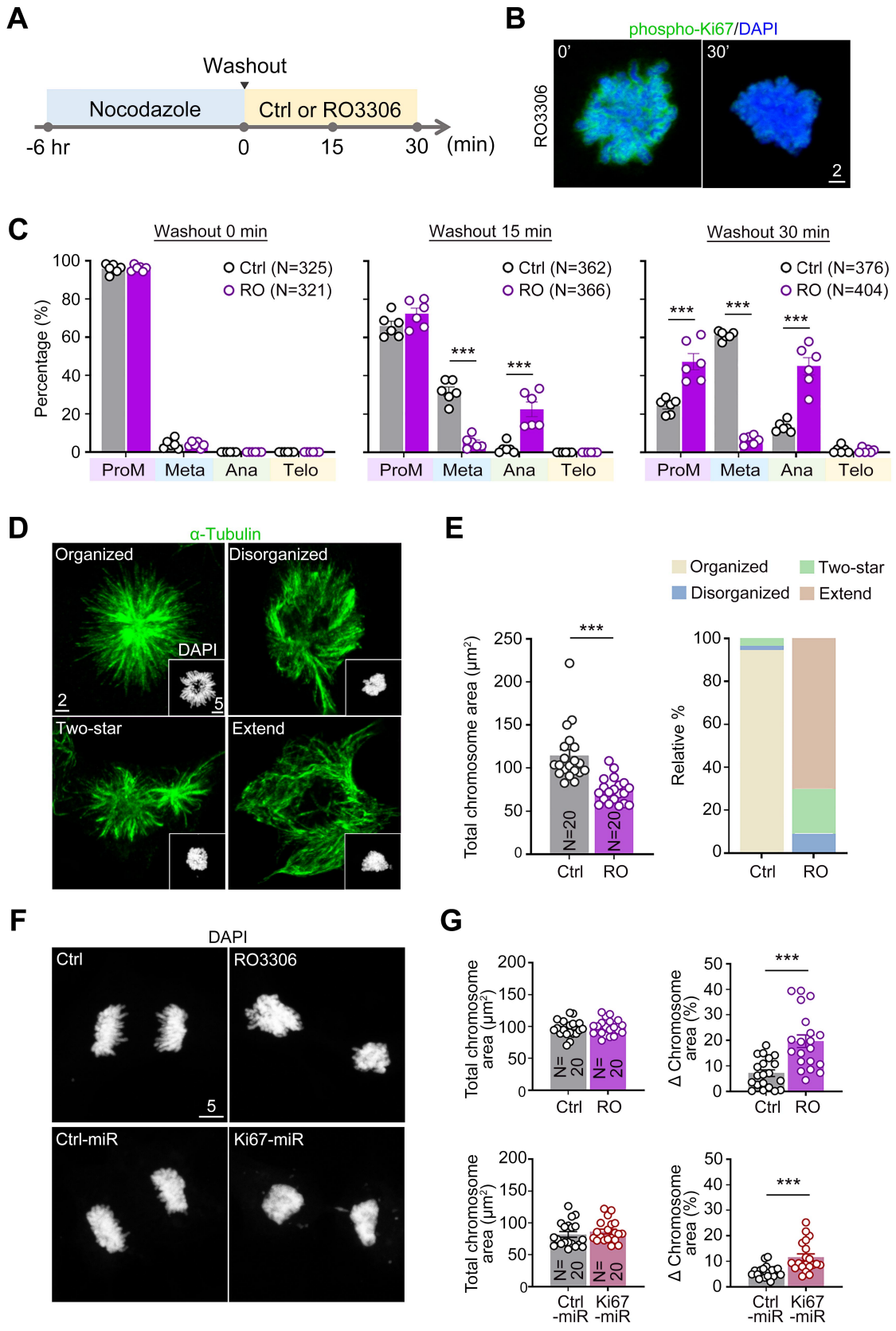
A
Washout
Nocodazole
Ctrl or RO3306
-6 hr
0
15
30
(min)
B
phospho-Ki67/DAPI
RO3306
0'
30'
2
C
Washout 0 min
Washout 15 min
Washout 30 min
Percentage (%)
Ctrl (N=325)
RO (N=321)
Ctrl (N=362)
RO (N=366)
Ctrl (N=376)
RO (N=404)
***
ProM
Meta
Ana
Telo
D
α-Tubulin
Organized
Disorganized
DAPI
Two-star
Extend
2
5
E
Organized
Two-star
Disorganized
Extend
Total chromosome area (μm²)
Relative %
N=20
Ctrl
RO
F
DAPI
Ctrl
RO3306
Ctrl-miR
Ki67-miR
5
G
Total chromosome area (μm²)
Δ Chromosome area (%)
N= 20
Ctrl
RO
Ctrl -miR
Ki67 -miR

813

814 **Figure 8.** A CDK1 inhibitor reduces Ki-67 phosphorylation, arrests mitotic progress and impairs
815 microtubule organization and sister chromatin separation.
816 (A) Experimental flowchart. Cells were treated with 50 nM nocodazole for 6 hrs to synchronize
817 the cell cycle at prometaphase. After removing nocodazole, cells were treated with 2 μM RO-3306
818 for 15 or 30 min and then harvested for immunostaining. Vehicle DMSO was included as a control
819 (Ctrl). Particular chromosome patterns determined mitotic stages. (B) RO-3306 treatment for 30
820 min reduces Ki-67 phosphorylation. (C) RO-3306 treatment disrupts mitotic progress. The
821 percentage of cells in metaphase was reduced, but the proportions of cells in prometaphase and
822 anaphase were increased. (D-E) Reduced Ki-67 phosphorylation disrupts chromosome and
823 microtubule organization. (D) Confocal images of chromosomes and microtubules at
824 prometaphase. Representative images of four types of Ctrl and RO-3306-treated cells are shown.
825 (E) Quantification of chromosome area and microtubule organization patterns. (F-G) Reduced Ki-
826 67 phosphorylation and Ki-67 protein levels both influence sister chromatin separation. (F)
827 Confocal images of chromosome arrangement in anaphase cells. Representative images showing
828 the effects of RO-3306 treatment and Ki-67 knockdown are shown. (G) Quantification of
829 chromosome area and the normalized difference in chromosome area between two daughter cells.
830 The sample size "N" indicates the number of examined cells. The data represent mean ± SEM and
831 individual data points are also shown. All data were collected from two independent experiments.
832 *** $P < 0.001$; unpaired two-tailed *t*-test. Scale bars: (C) whole cells: 2 μm; segment: 5 μm; (E) 5
833 μm.
834

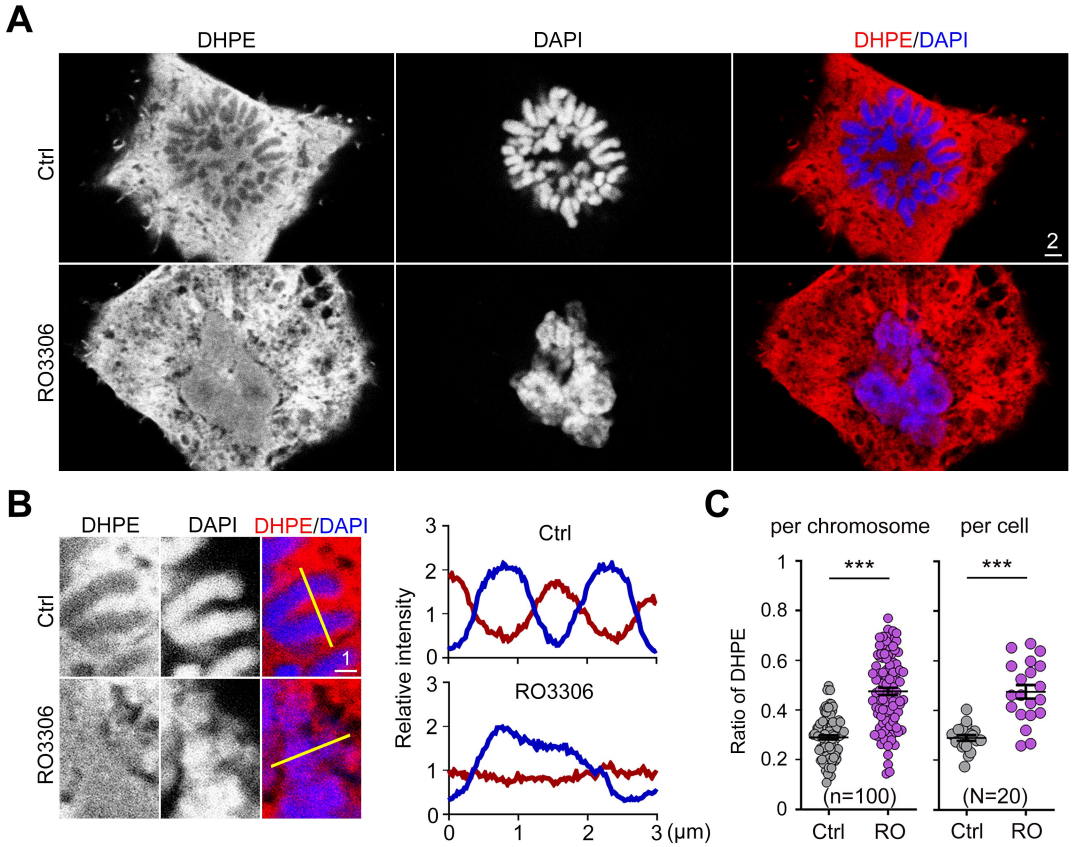

Figure 9. CDK1 inhibitor treatment alters nuclear lipid distribution.

COS-7 cells were treated with RO-3306 and then stained with biotin-DHPE, Ki-67 and DAPI. An LSM700 microscope was used to acquire images of the cells in prometaphase. (A-C) Reduced Ki-67 phosphorylation alters lipid distribution patterns. (A) Representative confocal images of biotin-DHPE in Ctrl and RO-3306-treated cells during prometaphase. (B) Line scanning analysis of biotin-DHPE distribution across the chromosome. The yellow line indicates the region subjected to line scanning. (C) Ratio of biotin-DHPE signal in the intrachromosomal area to that at the periphery. RO-3306 treatment enhanced intrachromosomal signals. The sample sizes "N" or "n" indicate the number of examined cells and chromosomes, respectively. The data represent mean ± SEM and individual data points are also shown. All data were collected from two independent experiments. *** $P < 0.001$; unpaired two-tailed *t*-test. Scale bars: (A) 2 μm; (B) 1 μm; (D) 2 μm.

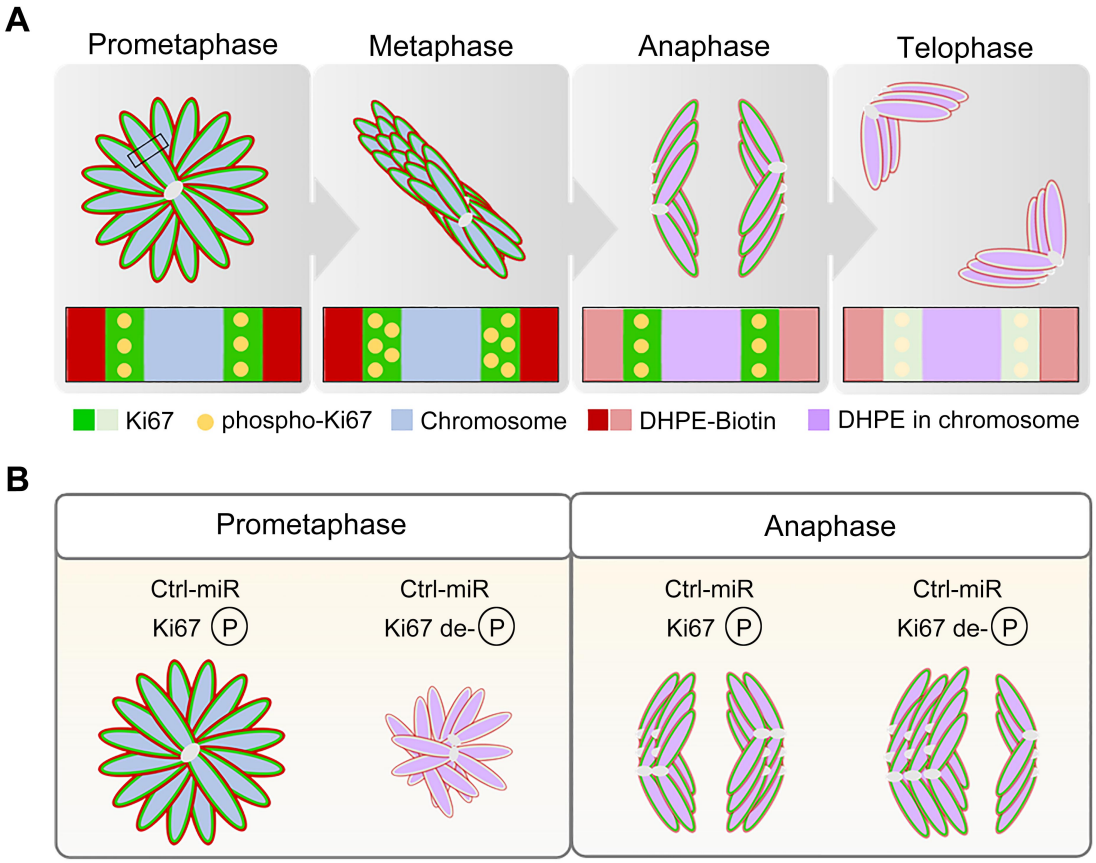

Figure 10. Dynamic alterations of nuclear lipids and Ki-67 phosphorylation and protein levels during mitosis. (A) Ki-67 regulates the distribution of nuclear lipids at the chromosomal periphery and forms the chromosomal envelope that regulates chromosome individualization during mitosis. (B) Ki-67 knockdown and Ki-67 dephosphorylation alter the lipid pattern at the chromosomal periphery and impair correct segregation of the sister chromatins.

Supplemental Information for

Ki-67 and CDK1 Control the Dynamic Association of Nuclear Lipids with Mitotic Chromosomes

Hsiao-Tang Hu[1], Ueh-Ting Tim Wang[2,3], Bi-Chang Chen[2], Yi-Ping Hsueh[1]*, Ting-Fang Wang[1]*

[1] Institute of Molecular Biology, Academia Sinica, Taipei, 11529, Taiwan; [2] Research Center for Applied Sciences, Academia Sinica, Taipei 11529, Taiwan; 3 Department of Photonics, National Yang Ming Chiao Tung University, Hsinchu 300093, Taiwan.

Supplemental Figure S1. Uncropped immunoblots of Figure 5B.

Supplemental Table S1. The numerical data for all figures.

Supplemental Table S2. All statistical results.

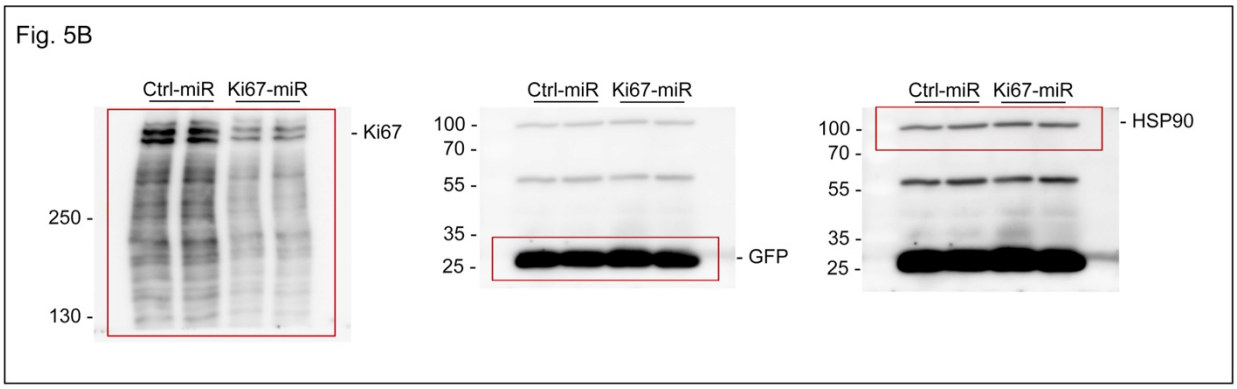

Supplemental_Fig_ S1. Uncropped immunoblots of Figure 5B.